JGR Atmospheres

RESEARCH ARTICLE
10.1029/2019JD031648

Key Points:

- Intraseasonal oscillations (ISO) in rainfall over the Bay of Bengal (BoB) propagate at a slower rate than over the Arabian Sea (AS)
- Differential atmospheric moisture flux convergence between BoB and AS determines the tilted structure of ISO
- The upper ocean in BoB and AS plays a more passive role in the tilt of the ISO

Correspondence to:
N. Karmakar,
nirupam.ju@gmail.com;
nkarmakar@fsu.edu

Citation:
Karmakar, N., & Misra, V. (2020). Differences in northward propagation of convection over the Arabian Sea and Bay of Bengal during boreal summer. *Journal of Geophysical Research: Atmospheres*, *125*, e2019JD031648. https://doi.org/10.1029/2019JD031648

Received 10 SEP 2019
Accepted 19 DEC 2019
Accepted article online 26 DEC 2019

Author Contributions
Conceptualization: Nirupam Karmakar, Vasubandhu Misra
Funding Acquisition: Vasubandhu Misra
Methodology: Nirupam Karmakar
Writing - Original Draft: Nirupam Karmakar
Formal Analysis: Nirupam Karmakar
Investigation: Nirupam Karmakar, Vasubandhu Misra
Project Administration: Vasubandhu Misra
Supervision: Vasubandhu Misra
Visualization: Nirupam Karmakar, Vasubandhu Misra
Writing - review & editing: Nirupam Karmakar, Vasubandhu Misra

Differences in Northward Propagation of Convection Over the Arabian Sea and Bay of Bengal During Boreal Summer

Nirupam Karmakar[1] and Vasubandhu Misra[1,2,3]

[1]Earth, Ocean and Atmospheric Science Department, Florida State University, Tallahassee, FL, USA, [2]Center for Ocean-Atmospheric Prediction Studies, Florida State University, Tallahassee, FL, USA, [3]Florida Climate Institute, Florida State University, Tallahassee, FL, USA

Abstract The governing dynamics that modulate the propagation characteristics of intraseasonal oscillations (ISO) during summer monsoon over the two ocean basins, Bay of Bengal (BoB) and Arabian Sea (AS), are investigated using observational analysis and high-resolution regional coupled ocean-atmosphere climate model simulations. ISO features are extracted over the Indian region using a data-adaptive spectral method called multichannel singular spectrum analysis. ISO exhibits stronger intensity over the BoB than over the AS. But ISO-filtered rainfall propagates at a faster rate (~1.25°/day) over AS as compared to BoB (~.74°/day), giving rise to a northwest-southeast tilted band of rainfall anomalies. However, the composite diagrams of several atmospheric fields associated with northward propagation like vorticity, low-level convergence, and oceanic variables like sea surface temperature and mixed layer depth do not show this difference in propagation speed and all exhibit a speed of nearly 0.75°/day in both the ocean basins. The difference in speed of ISO-filtered rainfall is explained through moisture flux convergence. Anomalous horizontal moisture advection plays a major role over AS in preconditioning the atmosphere and making it favorable for convection. Anomalous wind acting on climatological moisture gradient is the dominant term in the moisture advection equation. Easterly wind anomalies associated with a low-level anticyclone over India helps advect moisture from the eastern side of the domain. The northwest-southeast tilt of ISO is dictated by the atmospheric processes of moisture advection with the upper ocean playing a more passive role in causing the tilt.

1. Introduction

Indian summer monsoon rainfall shows a wide range of variability in both space and time with intraseasonal oscillations (ISO) representing a dominant mode of variability (Gadgil, 2003; Sikka & Gadgil, 1980; Webster et al., 1998; Yasunari, 1979). ISO in relation to Indian summer monsoon rainfall shows a dominant periodicity within 20- to 70-day timescale and is often associated with northward propagation of rainfall bands (Ajaya Mohan & Goswami, 2003; Karmakar et al., 2017; Krishnamurthy & Shukla, 2007; Sikka & Gadgil, 1980; Yasunari, 1979). Rainfall bands propagating from the equatorial region to the foothills of the Himalayas during summer monsoon are often linked with the northward migration of Intertropical Convergence Zone (ITCZ) (Sikka & Gadgil, 1980). These zonally oriented, northward propagating convective bands show a distinctive feature of northwest-southeast tilt over the Indian region (Karmakar et al., 2017; Krishnamurthy & Shukla, 2007; Lee et al., 2013). Active-break cycle of rainfall over India during monsoon season is often associated with the passage of these rainbands (Karmakar et al., 2017; Krishnamurthy & Shukla, 2007; Rajeevan et al., 2010). As ISO is governed by the internal dynamics that involves interaction between large-scale dynamics and organized convection, seasonal predictability of monsoon rainfall highly depends upon the contribution or the influence of ISO (Rajeevan, 2001; Sperber et al., 2001). However, our knowledge on the mechanism of the northward propagation of the ISO and the associated forecasting skills using dynamical models has been somewhat limited (D. Waliser et al., 2003; Sabeerali et al., 2013).

Many theories have been put forward to understand the basic structure and propagation mechanism of ISO since its discovery in the late 1970s. Wang and Xie (1997) proposed that northward propagation of ISO can be viewed as northwestward propagation of Rossby waves emanating from the equatorial Kelvin-Rossby wave packet over the Maritime Continent. The generation of Rossby waves are dependent upon the rapid decay of Kelvin-Rossby waves over the central Pacific. However, we do not have a proper understanding on why Rossby waves propagate northwestward. The importance of the generation of Rossby waves over the western Pacific in the northward propagation over the Indian region was also documented in many studies including Kemball-Cook and Wang (2001) and Annamalai and Slingo (2001). ISO is also viewed as a mode of variability possibly arising from internal atmospheric dynamics (D. Waliser et al., 2003; Fu & Wang, 2004; Jiang et al., 2004; Rajendran & Kitoh, 2006). Jiang et al. (2004) suggested that coupling between the free-atmosphere baroclinic and barotropic modes in the presence of strong vertical shear of the mean flow results in the generation of barotropic vorticity. This causes moisture convergence in the boundary layer to the north of an existing convection, which basically helps propagating the convection northward. DeMott et al. (2013) found that interaction between convection and mean state easterly and northerly shear induces an anomalous barotropic vorticity, which generates boundary layer moisture convergence to the north of convection. Boundary layer convergence forced by sea surface temperature (SST) gradients play secondary role in northward propagation over the Indian region. Alternatively, Webster (1983) claimed that northward propagation of convective maxima could possibly be a result of the north-south differential in total heating generated by surface hydrological feedback. It was further suggested that surface conditions at the lower boundary and atmospheric heating are strongly associated with the stability of the atmosphere, and thus convection. Changes in the surface conditions could result into changes in surface fluxes, which, in turn, alter the atmospheric heating gradient. This basically helps generating instability in the lower troposphere to the north of an existing convection and propagate the convective band northward (R. Nanjundiah et al., 1992; Srinivasan et al., 1993). B. Goswami and Shukla (1984) emphasized on the role of convective dynamical feedback process for northward propagation. In this case, convection increases static stability of the atmosphere and weakens the convection itself, while dynamic and radiative relaxation acts to bring the atmosphere to a convectively unstable state afterwards.

Air-sea interaction plays a crucial role in the northward march of convection (Kemball-Cook & Wang, 2001). Many studies report that high-resolution SST forcing is necessary to produce realistic ISO in models (Klingaman et al., 2008), while others suggest that high-frequency air-sea interaction could result in better ISO structures (Klingaman et al., 2011; Sharmila et al., 2013). In intraseasonal timescale, SST leads precipitation by around 10 days over the Indian Ocean (Achuthavarier & Krishnamurthy, 2011; Klingaman et al., 2008; Roxy et al., 2013). However, Roxy et al. (2013) suggested that this lead time is shorter over the Arabian Sea (AS) (5 days) compared to Bay of Bengal (BoB) (12 days). They analyzed rainfall as a convective response to the changes in SST anomalies and concluded that the presence of strong zonal gradient in SST over the AS increases surface convergence. This results in an accelerated upward movement of moisture and faster response to SST changes in terms of local rainfall anomalies. Few other studies suggest that SST-precipitation relationship is rather weak over the warm oceans and precipitation is largely modulated by the atmospheric dynamics (DeMott et al., 2013; Krishnamurthy & Kirtman, 2009; Rajendran et al., 2018).

In this study, the central question is based on understanding the structure of ISO over the Indian monsoon region, particularly over AS and BoB. More precisely, do we observe a difference in the propagation speed of ISO over the two ocean basins, namely, the AS and BoB. To this end, an investigation on the characteristics of ISO over the AS and BoB would provide an insight on the problem. Earlier studies have shown that moisture advection, specifically advection of climatological moisture by the anomalous wind from the northwest Pacific, is the principal factor in initiating the active or break conditions over India (Annamalai, 2010; Pillai & Sahai, 2014, 2016; Prasanna & Annamalai, 2012). Furthermore, moisture advection is found to lead rainfall by 8–9 days, whereas there is no lead-lag between rainfall and moisture convergence. Here, we investigate how moisture advection develops over AS and BoB before rainfall and how they contribute to the atmospheric instability using various observed and reanalysis products.

Alongside, we test the performance of a regional coupled model (RCM) in simulating the key aspects of ISO over AS and BoB. Although our understanding of ISO and its governing mechanisms have improved in recent times, modeling of ISO still remains a difficult task and many state-of-the-art models perform poorly in simulating the basic structure of ISO (Sabeerali et al., 2013; Sperber et al., 2013). Recently, usage of RCM has increased in view of enhanced representation of orography, coastlines, and land cover among many other factors, which enable better representation of seasonal mean and monsoon variability (Dash et al., 2006; Misra et al., 2018; Raju et al., 2015; Umakanth et al., 2016). Misra et al. (2018) investigated the performance of a high-resolution regional coupled ocean-atmosphere climate model and found that the model produces reasonable spatiotemporal structure, propagation characteristics, and amplitude of the ISO as compared to

Table 1
Physics Used in the RCM Simulation

Physics	References
Atmospheric component (RSM)	
Deep convection	Moorthi and Suarez (1992)
Shallow convection	Tiedtke (1983)
Clouds	Zhao and Carr (1997)
Boundary layer	Hong and Pan (1996)
Land model	Ek et al. (2003)
Gravity wave drag	Alpert et al. (1988)
Longwave radiation	Chou et al. (1999)
Shortwave radiation	Chou and Suarez (1994)
Oceanic component (ROMS)	
Mixing scheme	Mellor and Yamada (1982),Umlauf and Burchard (2003)
Boundary layer formation	*K*-profile (Large et al., 1994)

observations. In addition, this model also exhibits intraseasonal variations in SST and subsurface oceanic variables. We used this model for our study to not only compare the results with observations to examine the fidelity of the model in simulating the ISO characteristics over AS and BoB but also understand if upper-ocean stratification plays a role in the differential phase speed of ISO over the AS and BoB. In this study, the model simulations are performed at a grid spacing of 10 km. In the following two sections, we provide details of the model used and all the techniques adopted here, respectively. The results are described in section 3. A summary of the results and a short discussion is presented in section 4.

2. Data Sets and Methodology

2.1. Model Simulation

The Regional Spectral Mode l (RSM; atmospheric component) coupled with Regional Ocean Modeling System (ROMS; oceanic component) is used in this study as the RCM (H. Li & Misra, 2014; Misra et al., 2017, 2018). The RCM performs reasonably well in capturing the mean seasonal rainfall over the Indian region as well as the subseasonal variability (Misra et al., 2017, 2018). The circulation patterns associated with the active-break cycle over India are well simulated in the model. The RSM was first introduced in Juang and Kanamitsu (1994), and several modifications have been made to the model since then (Glazer & Misra, 2018; Kanamitsu et al., 2010; Misra et al., 2018). It has 28 terrain-following sigma vertical coordinates. The ROMS has 30 vertical sigma levels on a horizontal staggered Arakawa C grid (Shchepetkin & McWilliams, 2005). A summary of the physics used for the simulation is provided in Table 1. In this experiment, a 10-km grid resolution is used, and the grids are identical for both the RSM and ROMS. This enables direct exchange of fluxes between atmospheric and oceanic components without the need for interpolation. The coupling between ROMS and RSM occurs at 3-hr interval. Flux correction is not applied to the integration. The domain of integration is specified over the Indian region as shown in Misra et al. (2018) (roughly 4–37° N, 50–101° E). Lateral boundary conditions for the RSM are prescribed by the National Centers for Environmental Prediction-Department of Energy global atmospheric reanalysis (Kanamitsu et al., 2002) every 6 hr. The ROMS boundary forcings are from Simple Ocean Data Assimilation Version 2.2.4 (SODA v2.2.4), global oceanic analysis (Carton & Giese, 2008) prescribed at a monthly interval. The integration is carried out for a period of 10 years from 1 January 1986 to 31 December 1995.

2.2. Observed Data Set

Tropical Rainfall Measuring Mission (TRMM) 3B42 (V7) daily rainfall data (0.25° × 0.25°) for 1998–2014 (Huffman et al., 2007) have been used for this study. European Centre for Medium-Range Weather Forecasts (ECMWF) Re-Analysis (ERA)-Interim dataset (0.75° × 0.75°) (Dee et al., 2011) and the National Oceanic and Atmospheric Administration (NOAA) Optimum Interpolation Sea Surface Temperature (OISST) Version 2 daily data (0.25° × 0.25°) (Reynolds et al., 2007) are also used for the same period (1998–2014). Different fields from reanalysis data are obtained and daily averaging is done from the 6-hourly data. Mixed layer depth (MLD) climatology is obtained from mixed layer climatology and database (Holte et al., 2017) (http://mixedlayer.ucsd.edu/), which used over 1,512,000 Argo profiles to calculate MLD. The MLD is calculated using density threshold (Boyer Montegut et al., 2004). MLD is also calculated with the RCM output using the same methodology.

Daily climatology of the variables is calculated as the mean on each calendar day over the entire time period used in the analysis. Daily anomaly is then calculated by removing a smoothed daily climatology (using first two harmonics) from daily data.

2.3. Extracting ISO From Data

A data-adaptive filtering technique called Multichannel Singular Spectral Analysis (MSSA) is used to extract ISO features from the data in observations and model (Ghil et al., 2002; Plaut & Vautard, 1994). This technique is used in various studies specifically to extract oscillatory signals from short and noisy time series. It is also used extensively in monsoon studies to understand the structure of intraseasonal variability in rainfall (Karmakar et al., 2017; Karmakar & Krishnamurti, 2019; Krishnamurthy & Shukla, 2007; Moron et al., 2012). As a first step, we perform a prefiltering of the anomaly data with a 5-day moving mean to remove very high-frequency fluctuations possibly attributed to synoptic activities. These data for each year (May–October) are then fed into the MSSA algorithm to extract ISO. MSSA is applied to individual variables separately to examine ISO in each of these variables over the domain.

Since the shape and bandwidth of the filters in MSSA are functions of the data rather than prescribed by the user, it provides a superior way to extract signal from noise and identify anharmonic oscillations in a nonlinear system. A lag-covariance matrix is constructed by augmenting lagged copies of the data. This matrix is then diagonalized to obtain space-time empirical orthogonal functions (ST-EOFs) and space-time principal components (ST-PCs). The eigenvalues provide an estimate of the power in these modes. If two consecutive eigenvalues are nearly equal and their associated ST-EOFs and ST-PCs are in phase quadrature, then these two eigenmodes represent an oscillation (Plaut & Vautard, 1994). In this study, we use a lag window of 60 days while analyzing yearlong data, which provides sufficient confidence to extract ISO modes in the data (Plaut & Vautard, 1994). Additionally, a statistical test designed with 1,000 red noise surrogates is used to eliminate the possibility of detecting random fluctuations as oscillations (Allen & Robertson, 1996). Using the correct eigenmodes and associated ST-EOFs and ST-PCs, we can reconstruct part of the time series that explains a periodicity in the preferred range: the reconstructed components (RCs). We define ISO as the significant modes that have periodicity of 20–70 days. ISO is defined using an approach similar to that used in Karmakar et al. (2017) and Karmakar and Krishnamurti (2019). More details about the technique can be found in Ghil et al. (2002), and we refer to Karmakar et al. (2017) for details about how the technique is used on Indian monsoon rainfall to extract ISO modes. In the present study, MSSA is used to extract ISO from rainfall and other atmospheric and oceanic variables.

2.4. Moisture Flux Convergence Analysis and Moisture Budget

The propagation characteristics of ISO is studied using moisture flux convergence (MFC), which is a very useful derived parameter (from model output and observations) to understand convective initiation. The derivation and usefulness of MFC are discussed in detail in Banacos and Schultz (2005); here we provide a brief formulation of MFC.

MFC arises from the equation of conservation of water vapor in pressure coordinates:

$$\frac{1}{g}\int_{p_1}^{p_2}\frac{dq}{dt}dp = S, \tag{1}$$

where

$$\frac{d}{dt} = \frac{\partial}{\partial t} + u\frac{\partial}{\partial x} + v\frac{\partial}{\partial y} + \omega\frac{\partial}{\partial p}. \tag{2}$$

u, v, and ω, are zonal, meridional, and vertical components of wind in pressure coordinates (p), respectively, and q is specific humidity. S can be described as the difference between evaporation and precipitation. The left-hand side is a vertical integral from pressure level p_1 to p_2, and g is acceleration due to gravity. Using the mass continuity equation, equation (1) can be written as

$$\frac{1}{g}\int_{p_1}^{p_2}\left(\frac{\partial q}{\partial t} + \nabla\cdot(q\mathbf{V}_h) + \frac{\partial}{\partial p}(q\omega)\right)dp = E - P, \tag{3}$$

where E and P are evaporation and precipitation rates, respectively.

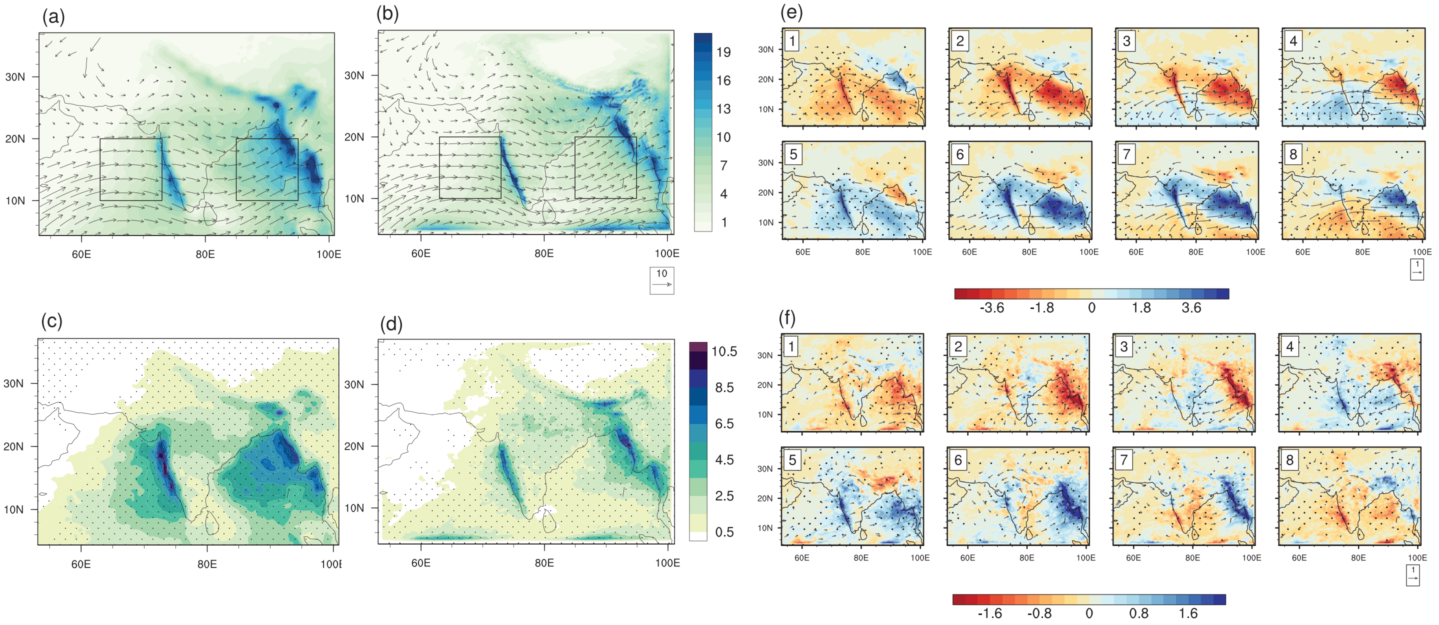

Figure 1. (a) May–October seasonal mean rainfall from 1998–2014 obtained from TRMM 3B42 rainfall. Vectors represent mean 850-hPa winds for the same time period from ERA-Interim reanalysis. (b) Same as (a) but for 10 years of model simulation. Boxes indicate the Arabian Sea (AS) and Bay of Bengal (BoB) boxes used in this study. (c) Spatial distribution of standard deviation of ISO-filtered rainfall for May–October 1998–2014 from TRMM 3B42 rainfall. (d) Same as (c) but for 10 years of model simulation. (e) Phase composite diagrams of ISO-filtered rainfall and 850-hPa wind anomalies during May–October 1998–2014. Phase compositing is done based a Principal Component Analysis (PCA)-based approach (see text for details). (f) Same as (e) but for 10 years of model simulation. Blue shades indicate positive rainfall anomalies, and red shades indicate negative anomalies. Units of rainfall and winds are mm/day and m/s, respectively. Stippled regions in (c)–(f) indicate values are significant at 5% level using a randomization test.

Equation (3) expresses the moisture budget for an air parcel, where $\nabla = \hat{\mathbf{i}}\frac{\partial}{\partial x} + \hat{\mathbf{j}}\frac{\partial}{\partial y}$ and horizontal wind field $\mathbf{V}_h = (u, v)$. The second term in the left-hand side of equation (3) describes horizontal moisture flux divergence. Therefore, negative of the second term is horizontal MFC. Henceforth, we simply call horizontal moisture flux convergence as MFC. Similarly, negative of the third term is vertical MFC (VMFC). The first term in equation (3) is the local rate of change of q. The right-hand side expresses the sources and sinks.

Horizontal MFC at any pressure level can be written as follows:

$$-\nabla \cdot (q\mathbf{V}_h) = -\mathbf{V}_h \cdot \nabla q - q\nabla \cdot \mathbf{V}_h = -u\frac{\partial q}{\partial x} - v\frac{\partial q}{\partial y} - q(\frac{\partial u}{\partial x} + \frac{\partial v}{\partial y}), \tag{4}$$

where the first two terms in the right-hand side of equation (4) represents the horizontal advection of moisture and the last term in the right-hand side is horizontal convergence of moisture. Therefore, MFC is a summation of horizontal moisture advection and moisture convergence. Further, vertical integration is performed from surface (p_2) to 200 hPa (p_1) level with a normalizing factor of g (=9.8 m/s) for each of these terms for analysis. Thus, MFC used in this study defined as

$$MFC = \underbrace{\left(\frac{1}{g}\int_{p_1}^{p_2} -(\mathbf{V}_h \cdot \nabla q)dp\right)}_{horizontal\ moisture\ advection} + \underbrace{\left(\frac{1}{g}\int_{p_1}^{p_2} -(q\nabla \cdot \mathbf{V}_h)dp\right)}_{horizontal\ moisture\ convergence}. \tag{5}$$

Similar to the other variables, we used MSSA to filter ISO signal from the MFC, horizontal moisture advection, and convergence data.

Further, a randomization test is used to perform statistical significance in the composite analysis using 1,000 bootstrap samples generated by randomly permuting the observed samples. The results are also tested using a student's t test for validation against a null hypothesis that the samples come from a population with zero mean (not shown). All the analyses presented here are consistent with both the significance tests.

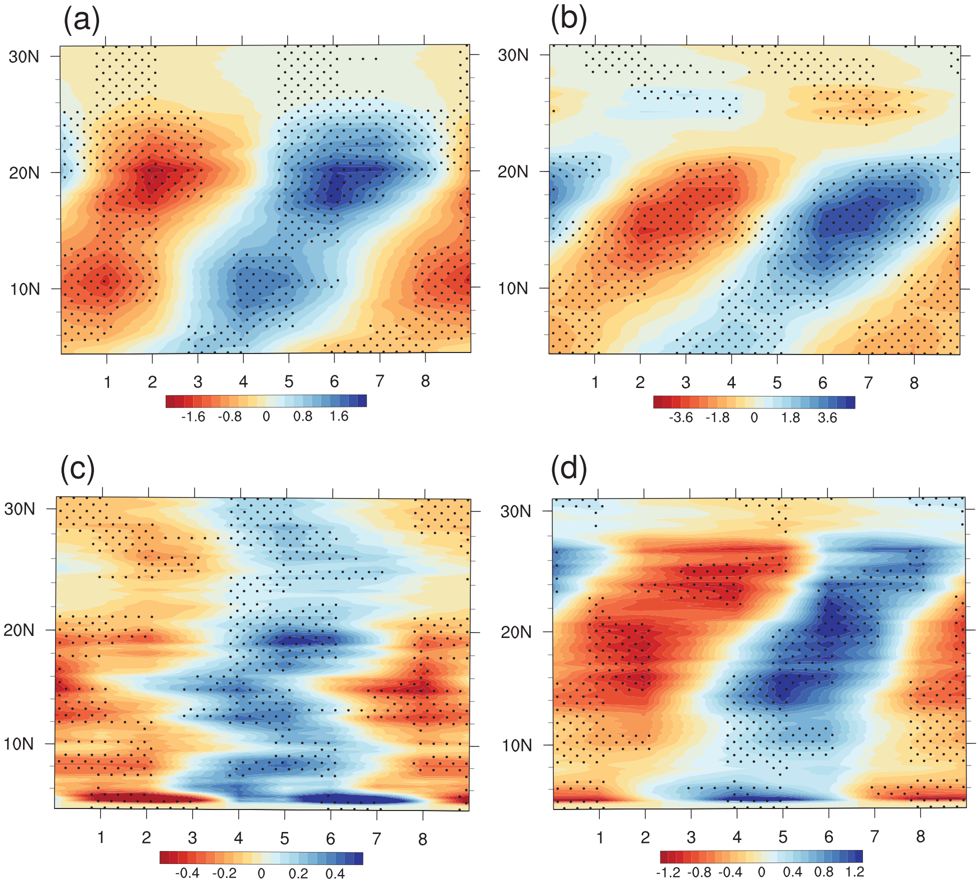

Figure 2. (a) Phase-latitude diagrams of ISO-filtered rainfall averaged over AS longitudes (63–73° N) during May–October 1998–2014. (b) Same as (a) but for BoB longitudes (75–85° N). (c) Same as (a) but for 10 years of model simulation. (d) Same as (c) but for BoB longitudes. Unit of rainfall is mm/day. Stippled regions indicate mean is significant at 5% level using a randomization test. Note that different scales in colorbars are used in different panels.

3. Results

3.1. ISO Features in the Model and Observations

Figures 1a and 1b show the May–October daily climatological rainfall and low-level winds patterns in observations and model, respectively. Rainfall amount nearly 15 mm/day is observed over the western Ghats, the foothills of the Himalayas, and Myanmar coast and northern BoB. Low-level westerlies are one of the basic characteristics of monsoon season. The model is able to capture these basic rainfall and wind structure, albeit with slightly weaker than observation rainfall over the northern BoB. It may however be pointed that TRMM rainfall 3B42 has some bias of showing excess rainfall near the mountains, especially in southeast Asia (Shige et al., 2017).

Intraseasonal features in the ISM rainfall during May–October are shown in Figures 1c and 1d for observations and the model, respectively. The spatial distribution of standard deviation of ISO-filtered rainfall anomalies for both observation and model are shown here. Strong intraseasonal activity is observed over the western Ghats, eastern AS, northern BoB, Burmese mountains, and coastal areas (Figure 1c). The model performs reasonably well in simulating the variability over central India, western Ghats, Burmese mountains, and coastal areas (Figure 1d). Further, we calculate eight phases of ISO to show its spatiotemporal evolution using a principal component analysis-based method (Karmakar et al., 2017; Moron et al., 1998) (Figures 1e and 1f). Essentially, the phase plane associated with the oscillation (ISO-filtered rainfall) is divided into eight equal intervals such that $-\pi + (m-1)\frac{\pi}{8} \le \gamma(t) < -\pi + m\frac{\pi}{8}$, $m = 1, \dots, 8$ ($\gamma(t)$ is phase angle, a function of time t). The average of ISO-filtered rainfall over all occurrences across all the years in any phase is called the phase composite for that particular phase. Figure 1e shows the 17-year average of phase composite for ISO-filtered rainfall and wind anomalies at 850-hPa level obtained from observations. The eight phases

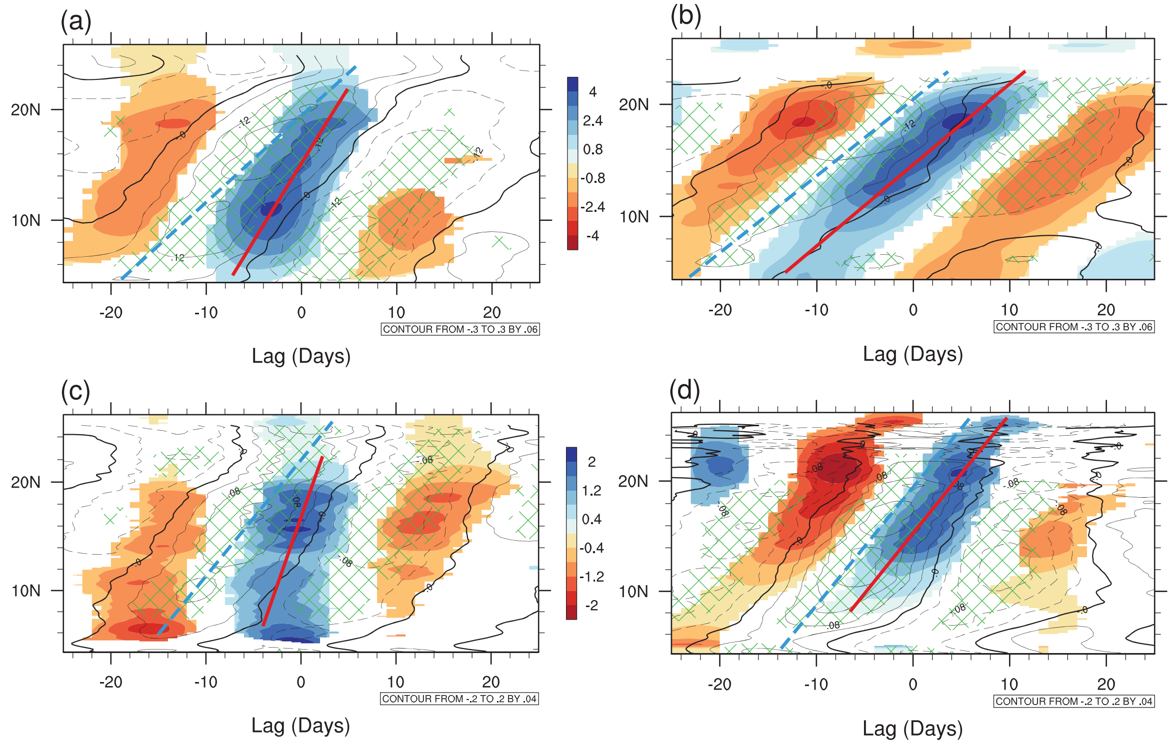

Figure 3. (a) Lag-latitude diagrams of ISO in rainfall (in colors) and ISO in SST (in contours; negative values in dashed contours) averaged over AS longitudes during the convective events (39 events). (b) Same as (a) but for BoB longitudes (63 events). (c) Same as (a) but for 10 years of model simulation (32 events). (d) Same as (c) but for BoB longitudes (30 events). Units of rainfall and SST are mm/day and K, respectively. Rainfall anomalies significant at 5% level using a randomization test are shown in colors. Green hatched areas show where SST is significant at 5% level. Red and dashed blue straight lines indicate estimated northward propagation of the averaged ISO anomalies of rainfall and SST, respectively.

are cyclic in order and are separated by an average of 4–5 days. In Phase 1, most of central and peninsular India is covered with a suppressed (negative) rainfall anomaly. In Phase 2, enhanced convection (positive rainfall) anomaly starts to develop over the southern Indian region, and negative anomaly gets established over central India. This is accompanied with an anticyclonic wind anomaly established over central India. In the subsequent phases, the positive ISO anomaly strengthens and moves northeastward and reaching central India and intensifying by Phases 6 and 7. Low-level winds exhibit strong cyclonic formation over central India in these phases. In Phase 8, the positive ISO band moves further northward and weakens over the foothills of the Himalayas. A northwest-southeast tilt in the convective band associated with ISO is seen (Phases 6 and 7). This canonical structure of ISO has been documented in many previous studies (Karmakar et al., 2017; Krishnamurthy & Shukla, 2007; Lee et al., 2013).

The model captures some aspects of the oscillatory behavior of ISO (Figure 1f). The BoB region shows strong positive anomalies in Phases 5 through 7, which subsequently propagates northward and weakens over the foothills of the Himalayas. However, ISO in the model is weaker in amplitude over the AS region as compared to the observations. The northwest-southeast tilt in the convection is comparatively less prominent in the model than in the observations. Simulating this tilt in the rain band associated with ISO is a difficult task, and many state-of-the-art models still fail to reproduce this band properly (Sabeerali et al., 2013). Figure 1f shows that RCM is capable of capturing the magnitude of the ISO anomalies over the Indian region.

The phase-latitude hovmoller diagrams of ISO during May–October 1998–2014 in TRMM rainfall over the AS longitudes (63–73° N) and BoB longitudes (75–85° N) are shown in Figures 2a and 2b, respectively. Clearly, ISO over the BoB is stronger than over the AS in observations (note that different scales are used in different panels for clarity). Northward propagation of convection is seen in both the ocean basins. Convection over the BoB is located at 6° N during Phase 4 and propagates northward to 20° N by Phases 7 and 8. However, this propagation seems faster over the AS region and reaches 20° N by Phase 6. This suggests that the propagation of convection appears to be faster over the AS than over BoB. This phenomena possibly gives rise to the tilted structure that we saw in the spatial patterns of ISO in Figure 1c. Our aim in this study

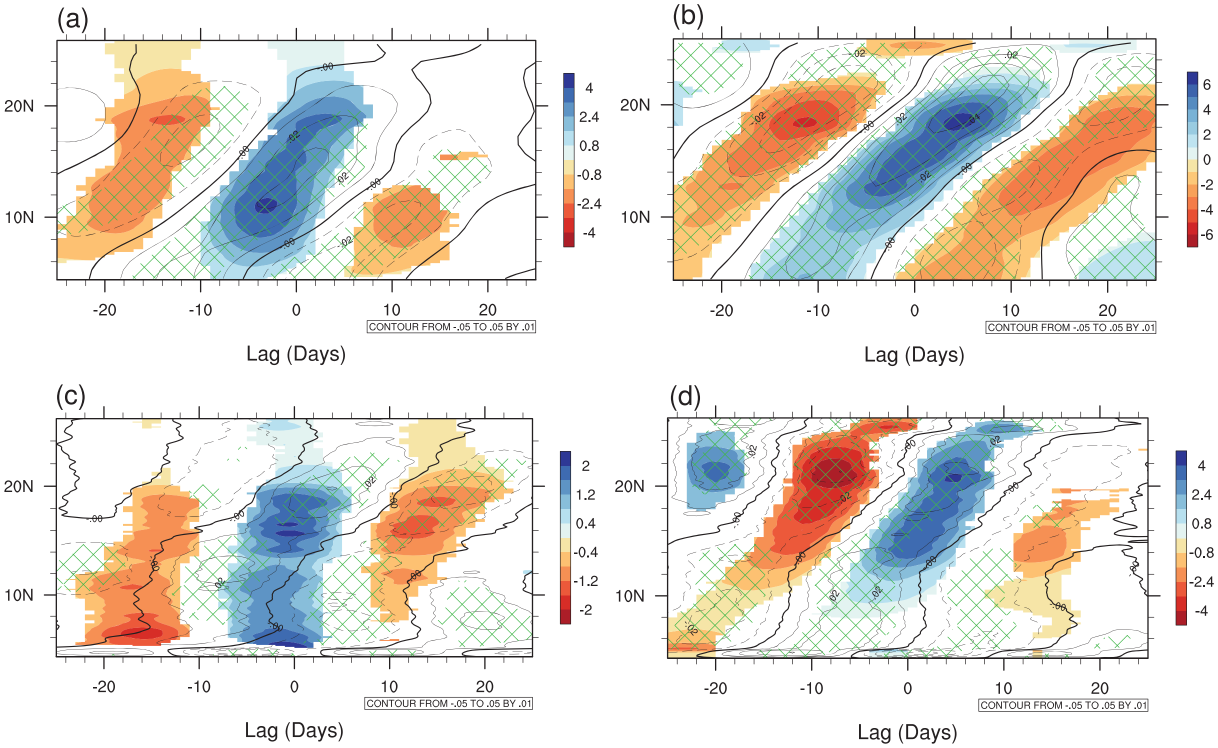

Figure 4. (a) Lag-latitude diagrams of ISO in rainfall (in colors) and ISO-filtered vertically integrated vorticity (in contours; negative values in dashed contours) averaged over AS longitudes during the convective events. (b) Same as (a) but for BoB longitudes. (c) Same as (a) but for 10 years of model simulation. (d) Same as (c) but for BoB longitudes. Units of rainfall and vorticity are mm/day and s^{-1}, respectively. Rainfall anomalies significant at 5% level using a randomization test are shown in colors. Green hatched areas show where vorticity is significant at 5% level.

is to understand what factors govern this difference in the speed to rainfall in ISO timescale. The model captures the propagation over the BoB region reasonably well (Figure 2d). However, the magnitude is lesser, and the propagation speed appears to be slightly faster in the model compared to observations (this aspect will be further analyzed in subsection 3.3). Although weak in magnitude, a faster northward propagation is seen over the AS region in the model, particularly between 15–25° N in the composite diagram during May–October for 10 years. Nevertheless, our main idea is to investigate why there is a difference in speed of propagation of ISO in the two oceanic basins. The model captures the seasonal mean and ISO propagation characteristics reasonably well, especially the differential speed of ISO in rainfall over AS and BoB.

3.2. Convective Events Over the AS and BoB

To understand the propagation characteristics better over the ocean basins, we identify the convective events associated with ISO over the BoB and AS. An area (10° × 10°) averaged ISO rainfall is taken into account over two boxes in the AS and BoB (outlined in Figure 1a), respectively. ISO-filtered rainfall data over these boxes are normalized by their corresponding standard deviation for every year. A convective event is identified if the normalized ISO rainfall anomaly exceeds +1 value. Sixty-three convective events are identified over the BoB, and 39 are found over the AS from the 17 years of TRMM rainfall data, whereas we found 30 convective events over the BoB and 32 events over AS in the 10 years of model simulation. Lag 0 (in days) is the day when the ISO rainfall is maximum over the particular box during each of these events in the AS or BoB. Positive lags indicate days after the convective maxima. Composite diagrams considering all the convective cases in each ocean basins for observations and model simulation, respectively, are created to investigate the propagation characteristics.

3.3. Northward Propagation of ISO

Figures 3a and 3b show the lag-latitude composite diagrams for observed ISO-filtered rainfall and SST during the convective events over AS and BoB, respectively. ISO in rainfall over the AS (in colors) shows much faster propagation speed than in the BoB. In both the ocean basins, SST leads the rainfall anomalies by few days. The lead in SST in intraseasonal timescale is reported in many previous studies

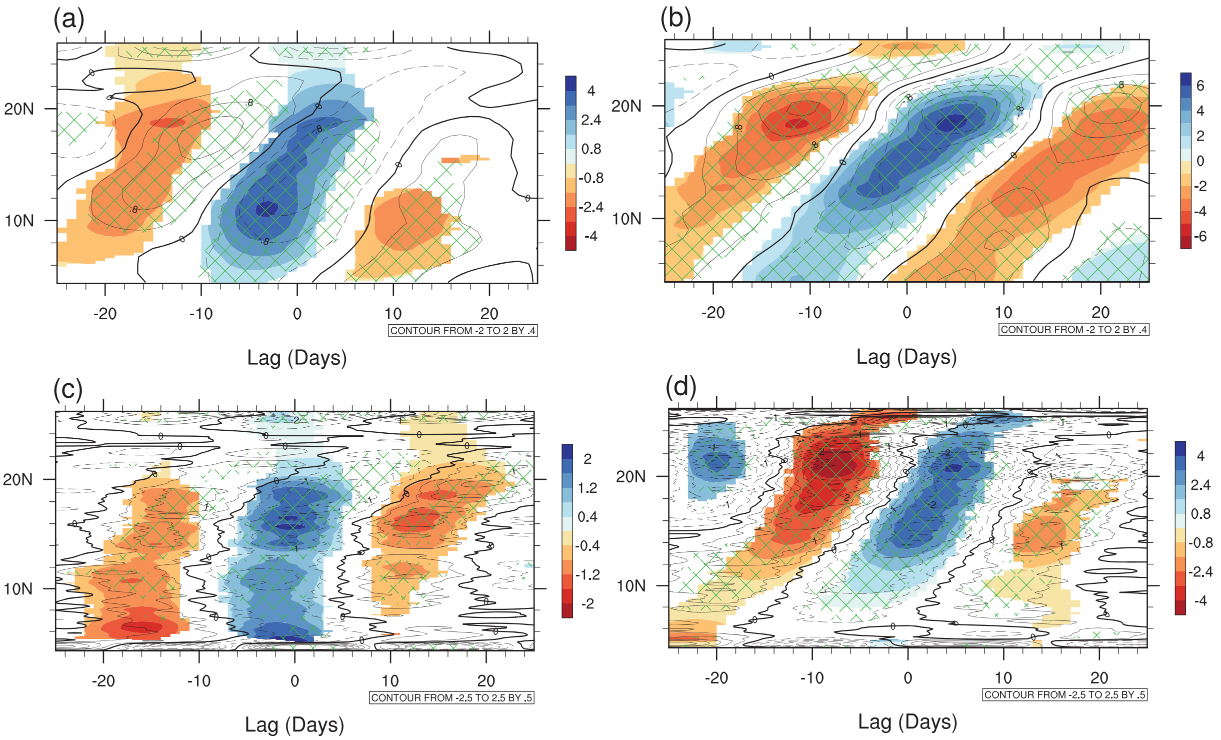

Figure 5. (a) Lag-latitude diagrams of ISO in rainfall (in colors) and ISO-filtered divergence at 925-hPa level (in contours; negative values in dashed contours) averaged over AS longitudes during the convective events. (b) Same as (a) but for BoB longitudes. (c) Same as (a) but for 10 years of model simulation. (d) Same as (c) but for BoB longitudes. Units of rainfall and divergence are mm/day and s^{-1}, respectively. Rainfall anomalies significant at 5% level using a randomization test are shown in colors. Green hatched areas show where divergence is significant at 5% level.

(Achuthavarier & Krishnamurthy, 2011; Klingaman, Weller, et al., 2008; Roxy et al., 2013). ISO in rainfall is demonstrated as a response to SST anomalies, and precipitation lags SST by nearly 5 days over the AS regions as compared to 12 days over the BoB (Roxy et al., 2013). Here, we found the amplitude of the observed SST variability at intraseasonal timescale is small (~0.15 K). The magnitude of variability is relatively higher in the AS side than in the BoB. The observed maxima in SST is found at nearly 17° N over the AS, but precipitation maxima is observed at 12° N (Figure 3a). However, the maxima in SST and precipitation both lie at around 19° N over the BoB (Figure 3b). We estimated the speed of northward propagation in rainfall and SST based on a regression technique (Appendix A). The speed of ISO in rainfall over the AS is nearly 1.25°/day, whereas SST propagates at a speed of 0.68°/day. However, the speed of SST and rainfall is nearly similar over the BoB. ISO-filtered rainfall and SST propagate at speed of 0.74 and 0.81°/day, respectively, over the BoB. Therefore, although there is not much difference in the speed of ISO in SST over the ocean basins, ISO in rainfall shows a significant difference in their propagation speed. This suggests that although precipitation lags SST nearly 10 days in the lower latitudes (below 10° N) in both the ocean basins, the lag reduces to almost 3–4 days in the northern AS.

The model captures the ISO characteristics over the ocean basins reasonably well during the convective events (Figures 3c and 3d). Especially, the difference in the speed of propagation between SST and rainfall over the AS is well captured in the RCM. ISO in rainfall and ISO in SST propagate at a higher speed in the model as compared to observations. Precipitation shows a propagation speed of nearly 2°/day over the AS and 1°/day over the BoB, whereas SST propagates at a speed of 0.9°/day over the AS and 1°/day over the BoB.

Northward propagation of ISO is often associated with genesis of barotropic vorticity in the presence of strong vertical shear of zonal winds (Jiang et al., 2004). The vorticity structure to the north of a convection center is essential to cause moisture convergence in the lower atmosphere, which helps the convective heating move northward. We investigate ISO-filtered vorticity anomalies during the convective events over the AS and BoB and found that the vertically integrated vorticity anomalies show nearly similar speed over the AS and BoB (Figures 4a and 4b). Vorticity and rainfall anomalies are nearly coincident over the BoB, which shows a prominent signal of northward propagation from the equatorial region to almost 25° N. However,

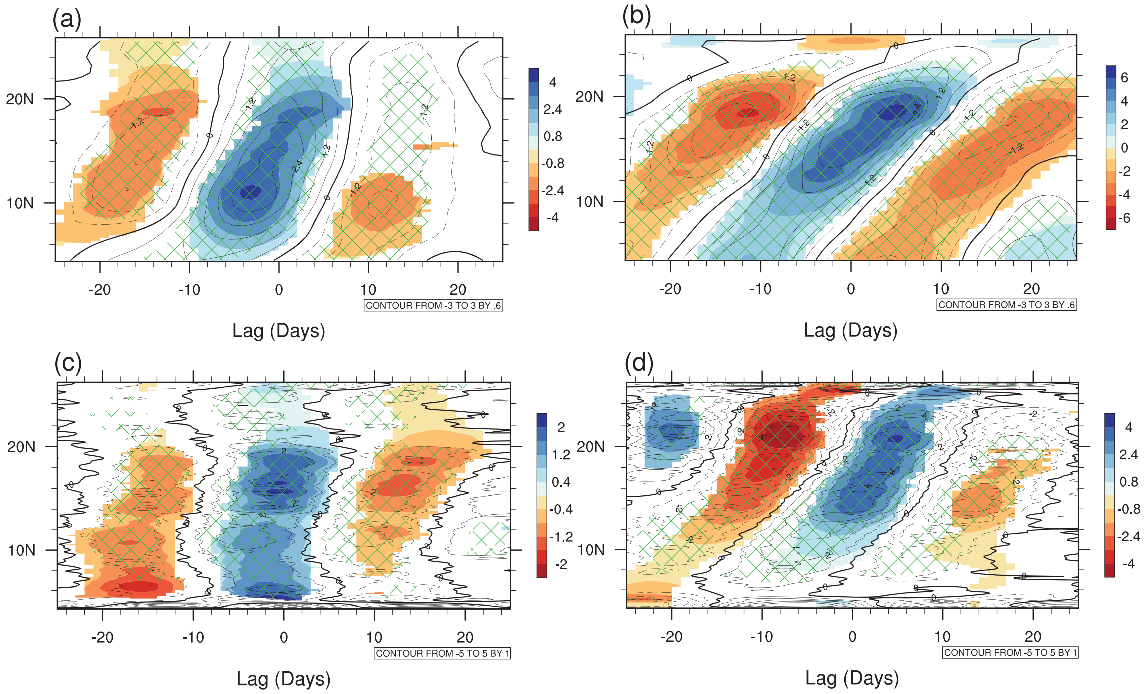

Figure 6. (a) Lag-latitude diagrams of ISO in rainfall (in colors) and ISO-filtered vertically integrated MFC (in contours; negative values in dashed contours) averaged over AS longitudes during the convective events. (b) Same as (a) but for BoB longitudes. (c) Same as (a) but for 10 years of model simulation. (d) Same as (c) but for BoB longitudes. Units of rainfall and MFC are mm/day. Rainfall anomalies significant at 5% level using a randomization test are shown in colors. Green hatched areas show where MFC is significant at 5% level.

precipitation and vorticity are observed to be propagating at a different speed over the AS. This suggests that the generation of barotropic vorticity mechanism may not be strongly modulating the rainfall at the intraseasonal timescale over the AS. This is further confirmed by the 925 hPa level divergence plots in Figures 5a and 5b. Low-level convergence acts to increase the low-level moisture, which enhances the low-level moist static energy to destabilize the atmosphere and move the convection northward (Kemball-Cook & Wang, 2001). Over the BoB, ISO-filtered low-level convergence shows very similar propagation speed and characteristics as rainfall (Figure 5b). However, low-level convergence shows different speed than ISO in rainfall over the AS, especially over the northern region (Figure 5a).

The model captures these structures reasonably well (Figures 4c, 4d, 5c, and 5d). Especially, the difference in speed between rainfall and vorticity over the northern AS region is well simulated in the RCM. Vorticity and low-level convergence show similar speed as rainfall over the BoB. Moreover, model-simulated variability in vorticity and convergence shows nearly similar magnitude as in observations. Therefore, both in model and observation it is found that the generation of barotropic vorticity and low-level convergence does not fully explain the speed of northward propagation of ISO over the northern AS region. This leads us to investigate further what other factors might modulate the propagation of ISO over AS.

In Figures 6a and 6b, we show the composite lag-latitude diagram of observed ISO-filtered vertically integrated horizontal MFC and rainfall anomalies over the AS and BoB, respectively, during convective events. It is observed that the MFC and rainfall show nearly similar speed of propagation over both the ocean basins. The maxima of both the variables are nearly overlapped, and MFC shows higher propagation speed over the AS compared to BoB. This suggests that convection over the northern AS region can be explained through the MFC. Rainfall over BoB is associated with both generation of barotropic vorticity and MFC. The RCM also captures this phenomena quite well (Figures 6c and 6d). MFC shows nearly similar structure as ISO in rainfall over both the ocean basins.

To summarize, we aim to calculate the phase speed of northward propagating ISO in both the ocean basins for observations and model using a regression technique discussed in Appendix A. Figures 7a and 7b show the phase speed of the calculated northward propagation of ISO for different fields (SST, convergence at 925 hPa, vertically integrated vorticity, MFC, and precipitation) over AS and BoB in observations and model,

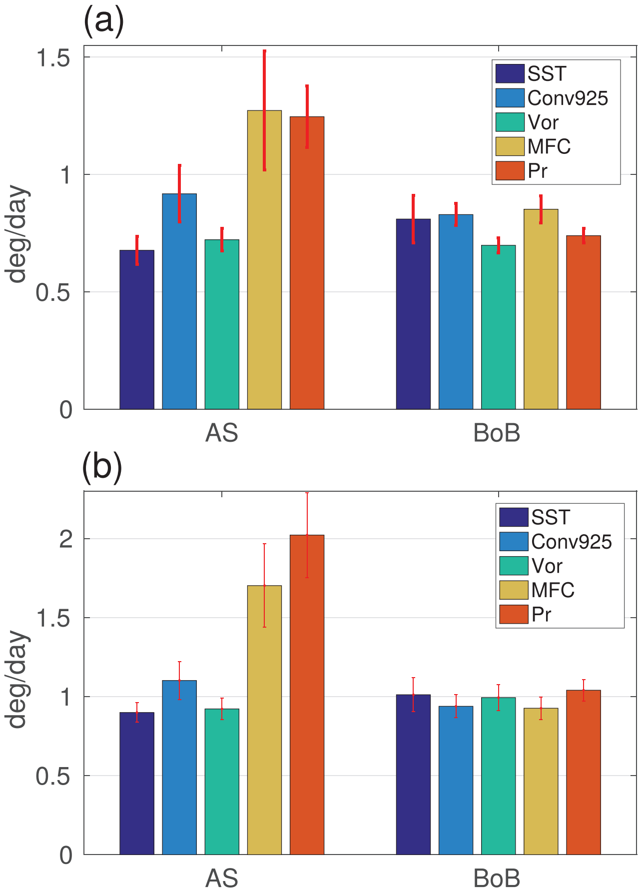

Figure 7. (a) Mean phase speed (in °/day) of northward propagation of different ISO-filtered sea surface temperature (SST), convergence at 925 hPa (Conv925), vertically integrated vorticity (Vor), moisture flux convergence (MFC), and precipitation (Pr) over the AS and the BoB longitudes between 5 and 30° N during the convective events in observations. (b) Same as (a) but for the model. Error bars indicate the spread of the values normalized by the number of samples. Note the different *y* axes in (a) and (b).

respectively. Clearly, rainfall over the AS shows much faster rate of propagation than over BoB, which is already documented in Figure 3. The model shows a good qualitative agreement on the speed of propagation of different fields over AS and BoB. However, the speed of almost all the fields calculated in the model appears to be somewhat faster than that in observations over both the ocean basins. MFC shows a good agreement with the speed of precipitation as seen in both model and observations, especially over AS. The bar plots presented in Figure 7 and hovmoller diagrams in Figure 6 suggest that MFC could be a key factor to modulate the rainfall over the northern AS.

3.4. Relation With the Surface Fluxes and Stability of the Atmosphere

Changes in surface heat fluxes and subsequent development of instability in the atmosphere are important factors in northward propagation of convection (R. Nanjundiah et al., 1992; Webster, 1983). Instability in the atmosphere can be determined using vertical moist stability (VMS), which is defined as the difference between vertically integrated moist static energy (MSE) of the top and the bottom of the atmospheric column ($MSE_{top} - MSE_{bot}$ with 600 hPa as the middle troposphere) (Neelin & Held, 1987). Increase in VMS indicates stability in the atmosphere and VMS below a certain threshold defines a necessary condition for the existence of convection in the tropics (Srinivasan & Smith, 1996). VMS shows a minima roughly around 10 days before strong convection maxima at intraseasonal timescale during Indian monsoon season (Karmakar & Krishnamurti, 2019). This suggests that VMS can be a good precursor of intraseasonal rainfall anomalies over the Indian region.

In Figures 8a and 8b, we show time series (ISO-filtered) of surface fluxes, zonal winds at 850 hPa (U850), SST, MFC, VMS, and precipitation averaged over the AS and BoB boxes, respectively, during convective events

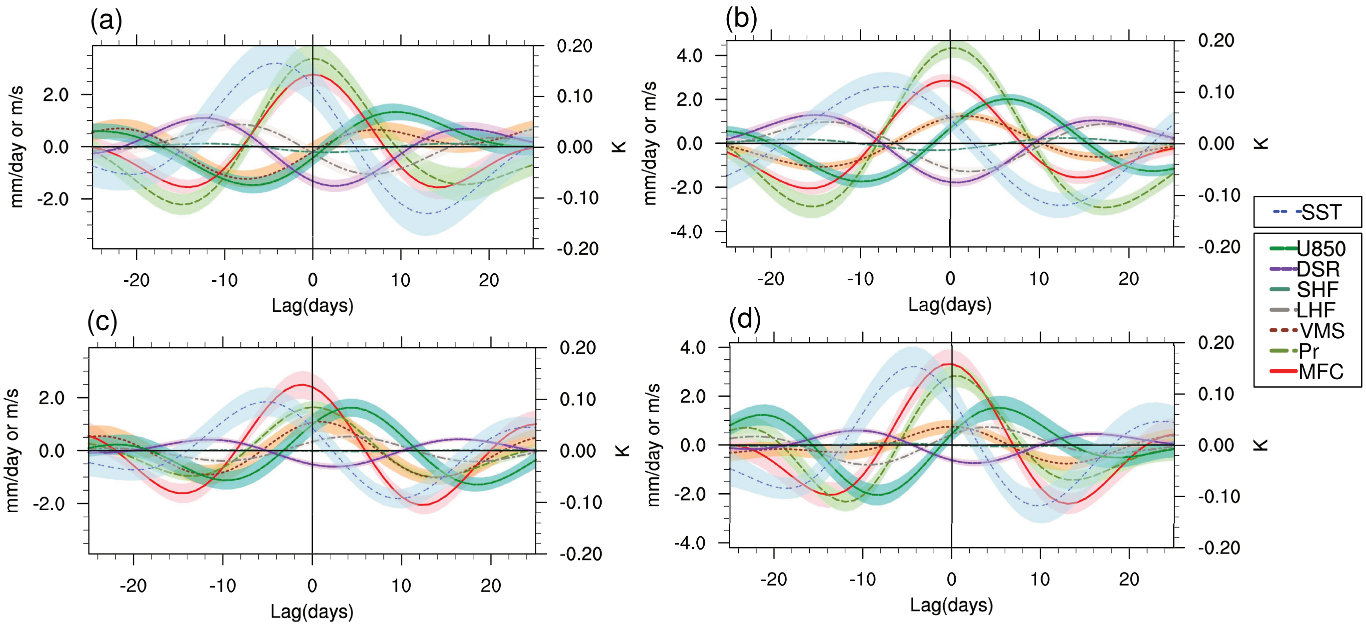

Figure 8. (a) Time series of different terms (ISO-filtered) during the convective events over the AS from observations. (b) Same as (a) but for BoB. (c) Same as (a) but for the model. (d) Same as (c) but for BoB. Units for surface downward shortwave radiation (DSR), upward sensible heat flux (SHF), upward latent heat flux (LHF), vertical moist stability (VMS), precipitation (Pr), and vertically integrated moisture flux convergence (MFC) are in mm/day (see Appendix **?** for conversion of units). Units of sea surface temperature (SST) and zonal wind at 850-hPa level (U850) are in K and m/s, respectively. Shading along each line indicates the spread of the values normalized by the number of samples. Note the difference in *y* axes in the panels.

in each of the ocean basins for observations. All the variables, except SST and U850, are converted to the unit of mm/day for better comparison (Appendix B). Lag 0 is the day when precipitation is maximum in the respective boxes. SST shows maxima around 4–5 days before rainfall maxima over AS. This lead in SST is even larger over BoB (7–8 days). Lesser lead time in SST over the AS was also noted in Roxy et al. (2013). They suggested the presence of a strong zonal gradient of SST over the AS accelerates the upward motion of the moist air, which results in a faster ocean-to-atmosphere response in terms of local rainfall anomalies. SST shows a sharp weakening immediately after precipitation maxima in both the ocean basins. The surface fluxes play a major role in the increasing and the decaying of the in situ SST anomalies. Intraseasonal downward shortwave radiation (DSR) anomalies show a peak value around 12 or 15 days before convection maxima over AS or BoB, respectively. Similarly, latent heat flux (LHF) attains a maxima immediately within 1–2 days after the maxima in DSR over BoB (Figure 8a). Over AS, the LHF maxima appears 4–5 days after the DSR maxima (Figure 8a). This is possibly associated with humidity and air temperature near the surface, as the availability of moisture in the lower levels is largely linked with the LHF. Although LHF is largely dictated by the surface winds (Gao et al., 2019; Raj Parampil et al., 2016), Raj Parampil et al. (2016) using satellite observations and ship-based data showed that the air temperature and moisture near the surface contribute as much as wind variability to LHF variability. These effects are more prominent away from the equator. Over BoB this effect can be seen more strongly as the peak in positive LHF (fluxes out of the ocean surface) appears nearly 3 days before the peak in low-level westerly U850 anomalies. The changes in LHF could thus be initiated by the changes in moisture and air temperature and then possibly enhanced by the low-level wind. This is supported by the changes in VMS, especially over BoB, which suggests that the atmosphere becomes unstable possibly because of enhanced supply of moisture and increased air temperature near the surface. VMS over the AS attains a minima (7 days before rainfall maxima) much later than over BoB (14 days before rainfall maxima). Thus, the atmosphere over BoB becomes unstable much before the AS. SST shows maxima soon after the low-level westerly wind reach its peak value over both the ocean basins. After the rainfall maxima over BoB, LHF, and VMS gradually become negative and positive, respectively (Figure 8b). This indicates that rainfall over the BoB stabilizes the atmosphere and reduces the surface fluxes and contributes to the decrease in SST, whereas LHF and VMS remain nearly zero during rainfall maxima over AS. MFC shows a close similarity with rainfall over AS as compared to BoB (Figure 8a). The

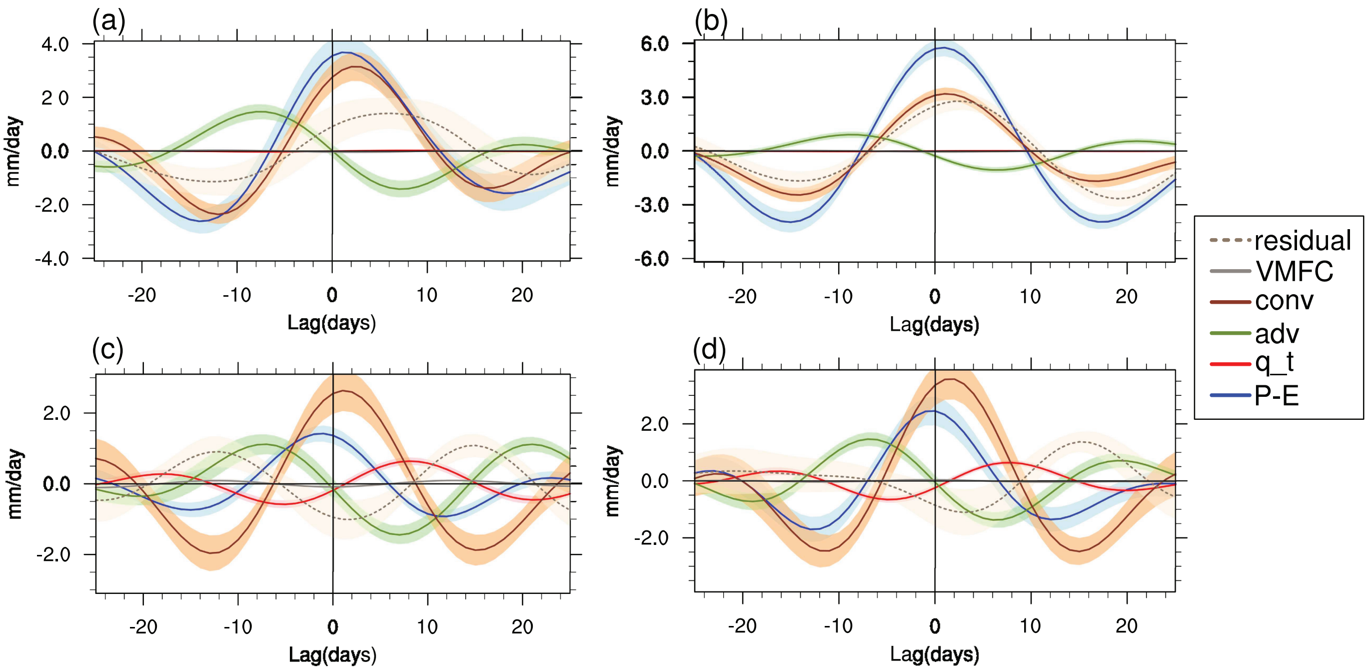

Figure 9. (a) Time series of different terms (ISO-filtered) of the moisture budget equation (terms in equation (6)) during the convective events over the AS from observations. (b) Same as (a) but for BoB. (c) Same as (a) but for model. (d) Same as (c) but for BoB. Units for precipitation-evaporation (P-E), horizontal moisture advection (adv), horizontal moisture convergence (conv), vertical MFC (VMFC; nearly zero in all cases), and moisture tendency (q_t) are given in mm/day. Shading along each line indicates the spread of the values normalized by the number of samples. Note the difference in y axes in the panels.

rainfall maxima at Lag 0 is largely explained by MFC over the AS. Sensible heat flux (SHF) anomalies show negligible changes during these convective events over both the ocean basins.

The RCM captures the variations in rainfall and MFC reasonably well (Figures 8c and 8d). However, MFC shows higher values than rainfall anomalies during Lag 0 over both the ocean basins. The lead of SST anomalies on rainfall anomalies over BoB is relatively less in the RCM as compared to observations. The magnitude of intraseasonal variations in the DSR anomalies is also lesser in the RCM. LHF is not well captured in the model and shows negative values a week before rainfall maxima, which gradually becomes positive and attains maxima after Lag 0 over both the ocean basins. VMS shows very weak variability over AS and remains negative during Lag 0. VMS becomes positive over BoB during rainfall maxima. SHF shows negligible values during these events over both AS and BoB. Thus, the intraseasonal variability of rainfall in the model is well explained by MFC in the RCM. Next, we aim to identify how MFC modulates rainfall by looking into each terms in the MFC equations (equations (3) and (5)).

3.5. MFC Budget

Given the fact that the MFC closely resembles the rainfall patterns (Figures 6–8), and the faster propagation speed over the AS is explained by the propagation of MFC, we aim to analyze the MFC budget equation and understand the relative roles of the individual terms. Equation (3) represents the budget equation for MFC. Performing ISO filtering in both sides of the equation and using equation (5), equation (3) can be written as

$$\left(\frac{1}{g}\int_{p_1}^{p_2} -\frac{\partial q}{\partial t}dp\right)' + \left(\frac{1}{g}\int_{p_1}^{p_2} -(\mathbf{V}_h \cdot \nabla q)dp\right)' + \left(\frac{1}{g}\int_{p_1}^{p_2} -(q\nabla \cdot \mathbf{V}_h)dp\right)' + \left(\frac{1}{g}\int_{p_1}^{p_2} -\frac{\partial}{\partial p}(q\omega)dp\right)' + residual = (P-E)', \tag{6}$$

where (′) denotes ISO-filtered quantities. In Figure 9, we show different terms in equation (6) for both observations and model. Second and third terms in the left-hand side of equation (6) represent horizontal moisture advection and convergence, respectively. A residual term appears possibly because of interaction between different timescales. In observations, the intraseasonal variations in precipitation-evaporation (P-E) is largely balanced by intraseasonal variations in horizontal moisture advection (adv) and moisture convergence (conv) (Figures 9a and 9b). Both local rate of change of humidity (q_t) and vertical MFC (VMFC)

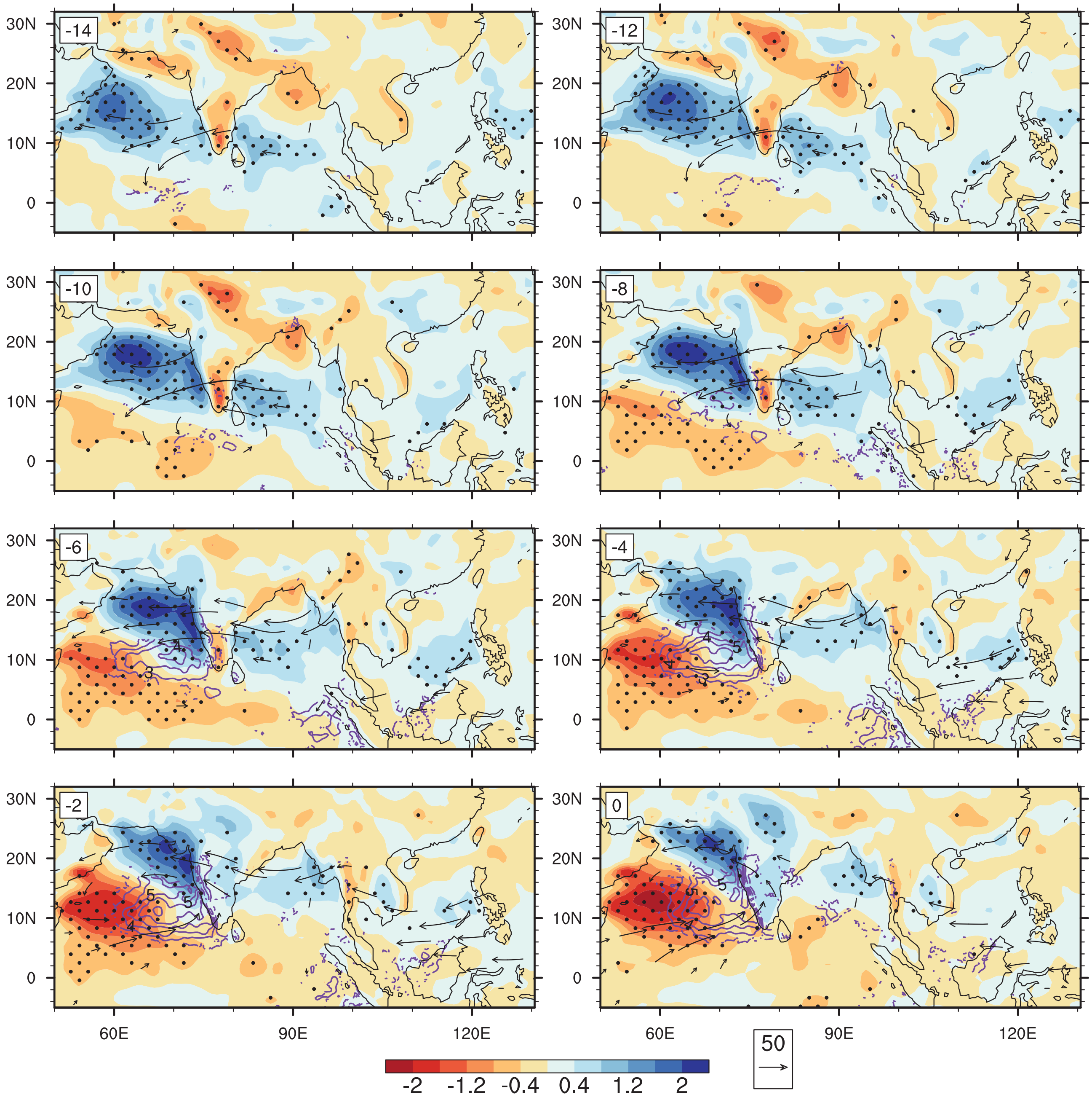

Figure 10. Composite maps of ISO-filtered moisture advection anomalies (colors; in mm/day), positive rainfall anomalies (purple contours with contour interval 1; in mm/day), and moisture transport vector anomalies (in kg·m^{-1}·s^{-1}) at different lags during the convective events over the AS from observations. Numbers in the panels mark different lags (in days) before the convective maxima (Lag 0). Stippled regions indicate mean is significant at 5% level using a randomization test. Only significant rainfall anomalies and vector anomalies are shown here.

are negligibly small during the convective events over AS and BoB. However, moisture advection over AS shows stronger variability than BoB and shows a peak almost a week before the rainfall maxima. Therefore, moisture advection could possible play a stronger role in modulating the behavior of rainfall over the AS compared to BoB. RCM captures this lead in advection quite well, however, the magnitude of variability in advection term shows nearly similar magnitude over both the ocean basins (Figures 9c and 9d). Further, the convergence term in the model shows stronger amplitude than in observations. Although the vertical MFC term is negligible, local rate of change of humidity shows comparable variability during these events in the model.

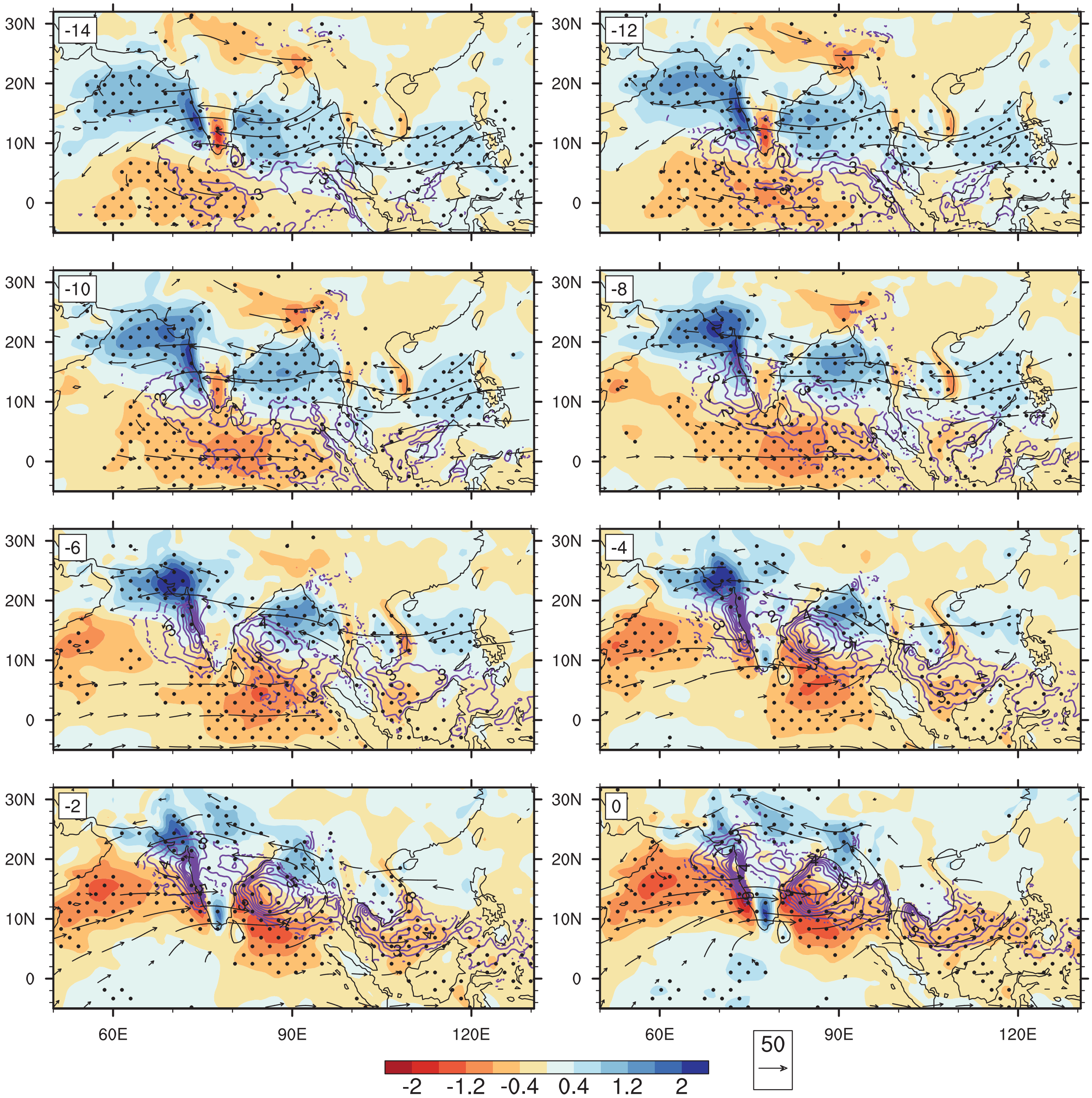

Figure 11. Same as Figure 10 but during observed convective events over BoB.

The above discussion suggests that the development of horizontal moisture advection is of larger amplitude over the AS and could be an important factor in premoistening the atmosphere for convective activity over the northern AS. To better understand how moisture advection builds up over this region, we investigate the spatial maps of ISO-filtered horizontal moisture advection and vertically integrated moisture transport vectors ($\mathbf{V} \cdot q$). Figure 10 shows the maps of these fields at different times before the rainfall maxima over the AS box in observations. Two weeks before the rainfall maxima, advection shows positive anomalies over the AS region, which is also evident from Figure 9a, and the vectors show anomalous moisture transport to the west of the AS from the east. Positive anomalous moisture advection over a region means anomalous moisture is being advected to that particular region. This moisture advection before the convection maxima is supported by strong low-level anomalous easterlies as seen from the phase composite diagrams in Figure 1e (Phases 3–5)). By 10 days before the rainfall maxima, the signals are strengthened, and moisture

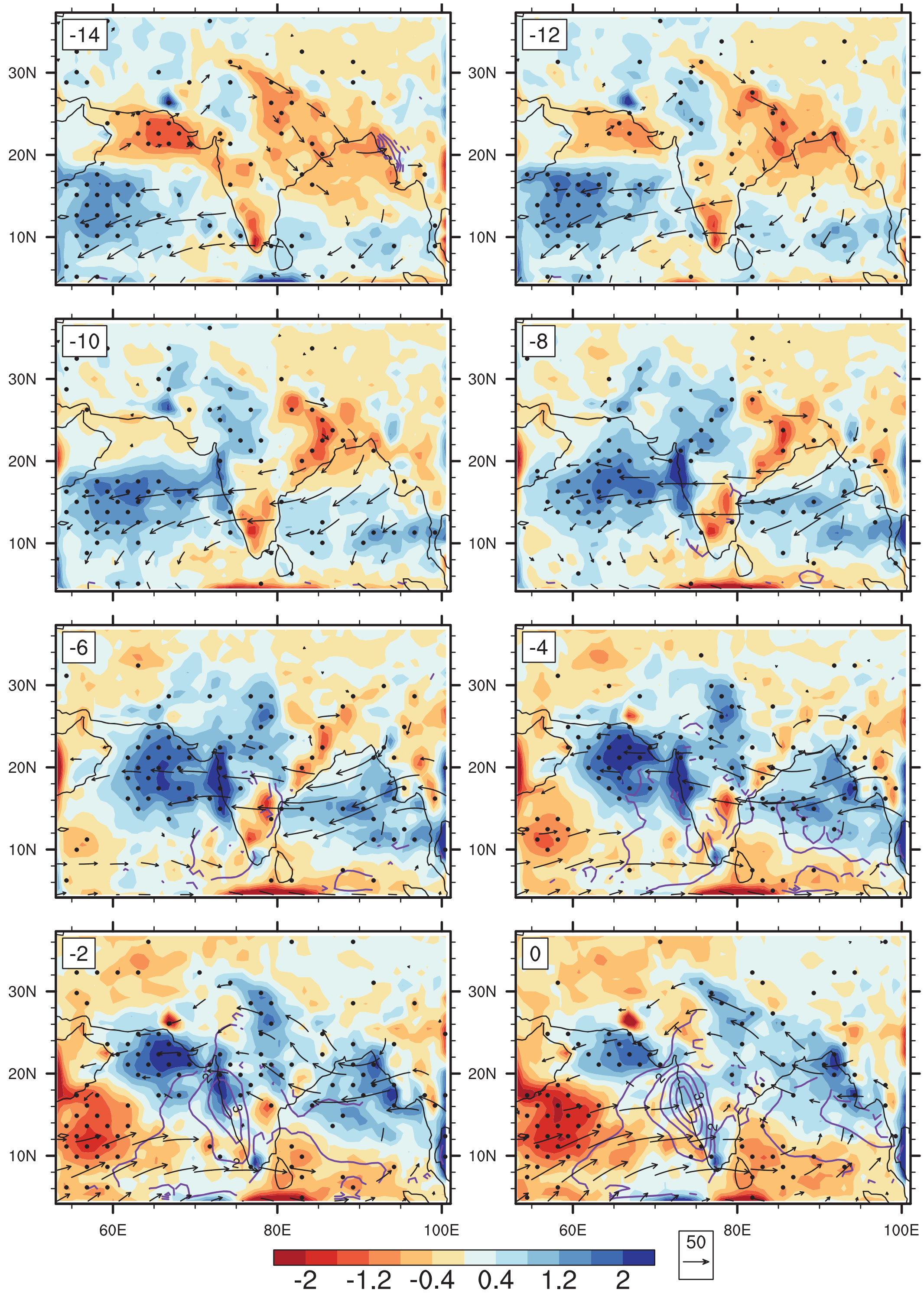

Figure 12. Composite maps of ISO-filtered moisture advection anomalies (colors; in mm/day), positive rainfall anomalies (purple contours with contour interval 1; in mm/day), and moisture transport vector anomalies (in kg·m^{-1}·s^{-1}) at different lags during the convective events over the AS from the RCM. Numbers in the panels mark different lags (in days) before the convective maxima (Lag 0). Stippled regions indicate mean is significant at 5% level using a randomization test. Only significant rainfall anomalies and vector anomalies are shown here.

advection shows a maxima over the AS by Lag (−8). Strong moisture advection associated with anomalous easterly transport of moisture is observed during Lags (−8) to (−4) over the northern AS region. At Lag 0, a cyclonic structure is established over the AS region with negative moisture advection over the south and positive over the north of AS. On the other hand, a strong anticyclonic structure in moisture transport vectors is established over the central Indian region 2 weeks before the rainfall maxima over BoB (Figure 11). This structure resembles the low-level anticyclone during break phases of monsoon. During Lags (−10) and (−6), moisture transport vectors show anomalous moisture being transported from South China Sea toward the Indian region. Positive moisture advection anomalies are observed over BoB associated with strong easterly anomalies over BoB during this period. By Lag (−4), a cyclonic structure starts to establish over peninsular India flanked toward both oceanic sides. A northwest-southeast oriented tilt is noted in this formation, as moisture advection maxima is observed over the northwestern India and Pakistan region. Gradually, a cyclonic structure is established by Lag 0 over India. Contrary to the AS case (Figure 10), the center of the cyclonic structure in the BoB case is located over central India (Figure 11). The westerly moisture transport vectors at nearly 15° N in Lag 0 crosses peninsular India and extends to central BoB before turning northward during the convective events over BoB. These spatial maps of moisture advection also show that the magnitude of variability is comparatively weaker over BoB than in AS.

RCM captures the large-scale structure in moisture advection anomalies reasonably well (Figures 12 and 13). The development of strong positive moisture advection anomalies with westward anomalous moisture transport vectors are observed during Lags −10 through −4 during convective events over the AS (Figure 12). Similar to observations, the easterly transport vectors gradually propagate northward and a large-scale cyclonic vortex is established over India during Lag 0. During the BoB convective events, similar development of moisture advection over the Indian region with westward moisture advection is seen over the BoB and AS during Lags −10 through −6 (Figure 13). Cyclonic vortex is well established by Lags (−2) and 0 over India. These spatial maps of anomalous moisture advection and transport vectors in both observations and the RCM suggest that the source of this anomalous moisture over AS and BoB is from the east and low-level anomalous flow carries this moisture toward this region, which helps generating the instability. The strongest signature of moisture advection is seen over the northern AS region in both model and observations a few days before the rainfall maxima. This suggests that instability in the atmosphere over AS is strongly associated with this moisture advection (Figures 8a and 9a), as intraseasonal VMS decreases immediately after moisture advection peaks nearly almost a week before the rainfall maxima. However, instability over BoB grows in the atmosphere few days ahead of the moisture advection maxima (Figures 8b and 9b). This instability over BoB is closely associated with the surface latent heat flux, implying that convection over BoB is more influenced by local surface fluxes rather than moisture transport from a distant location. Whereas AS rainfall is largely modulated by the moisture advection and thermodynamics over the region, and soon after the moisture advection reaches its maxima, atmosphere becomes unstable and convection starts. This possibly suggests that the ocean-atmosphere coupling might be stronger over the BoB, which could act to slow down the speed of northward propagation. Therefore, we observe a faster propagation speed of intraseasonal rainfall over AS.

3.6. Moisture Advection

Now that we have identified the dominance of moisture advection during and before the rainfall maxima over AS, we now examine relative contribution from horizontal wind and moisture gradient. The anomalous ISO-filtered moisture advection (ISO-filtered quantity of the first term in the right-hand side of equation (5)) can be partitioned into different components as follows:

$$\begin{aligned}\left(\frac{1}{g}\int_{p_1}^{p_2} -(\mathbf{V}_h \cdot \nabla q)dp\right)' = &\frac{1}{g}\int_{p_1}^{p_2}(-\mathbf{V}_h^c \cdot \nabla q')dp + \frac{1}{g}\int_{p_1}^{p_2}(-\mathbf{V}'_h \cdot \nabla q^c)dp \\ &+ \frac{1}{g}\int_{p_1}^{p_2}(-\mathbf{V}'_h \cdot \nabla q')dp + residual,\end{aligned} \tag{7}$$

where ($'$) denotes ISO-filtered quantities and quantities with superscript c are climatological mean fields (based on May–October values). All the terms are vertically integrated from surface (p_2) to 200 hPa (p_1). The left-hand side represents the ISO-filtered moisture advection term that is discussed in the previous sections. The first term on the right-hand side ($\frac{1}{g}\int_{p_1}^{p_2}(-\mathbf{V}_h^c \cdot \nabla q')dp$) denotes advection associated with the climatological horizontal wind acting on ISO-related anomalous moisture gradient. The second term

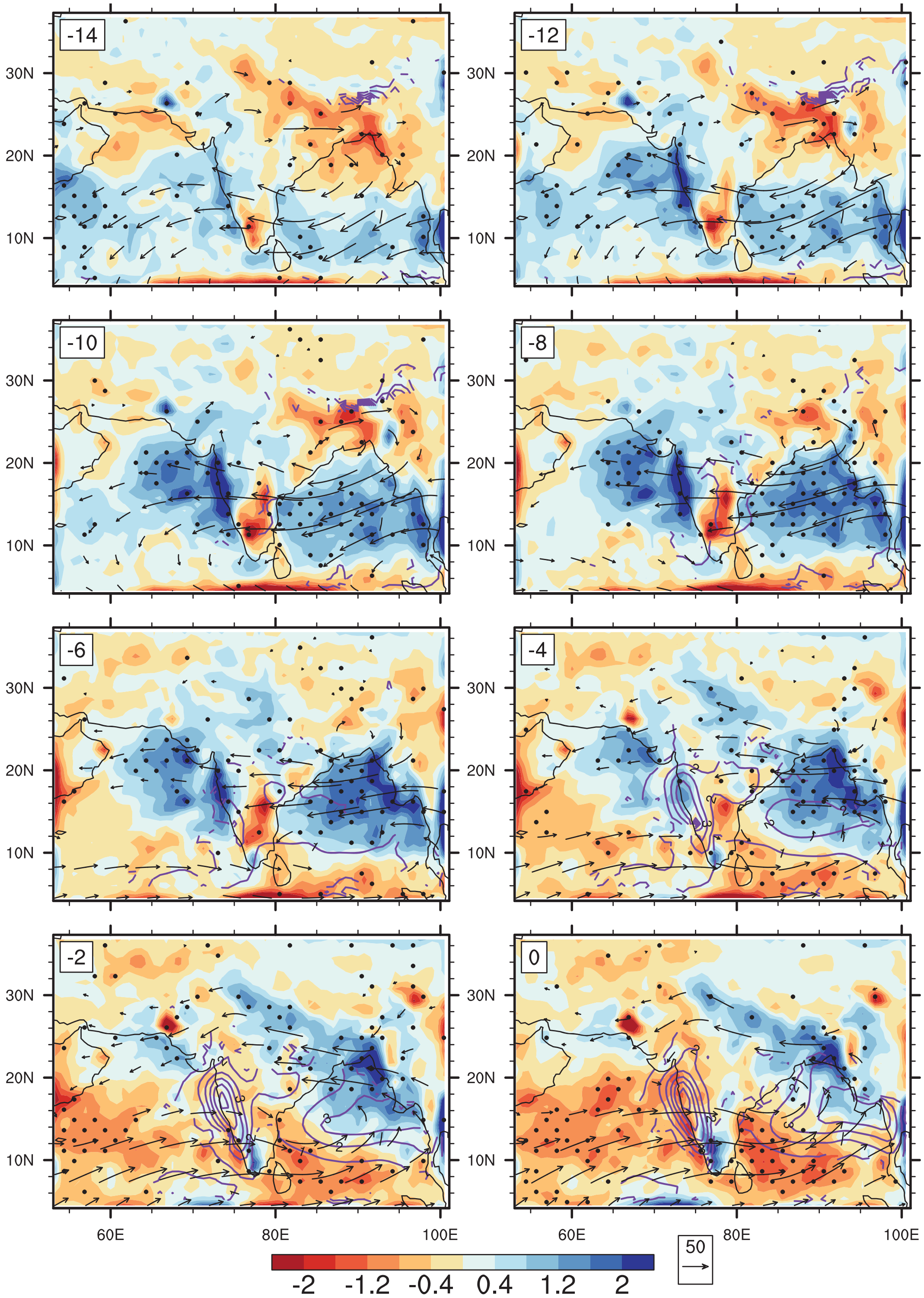

Figure 13. Same as Figure 12 but during convective events over BoB in the RCM.

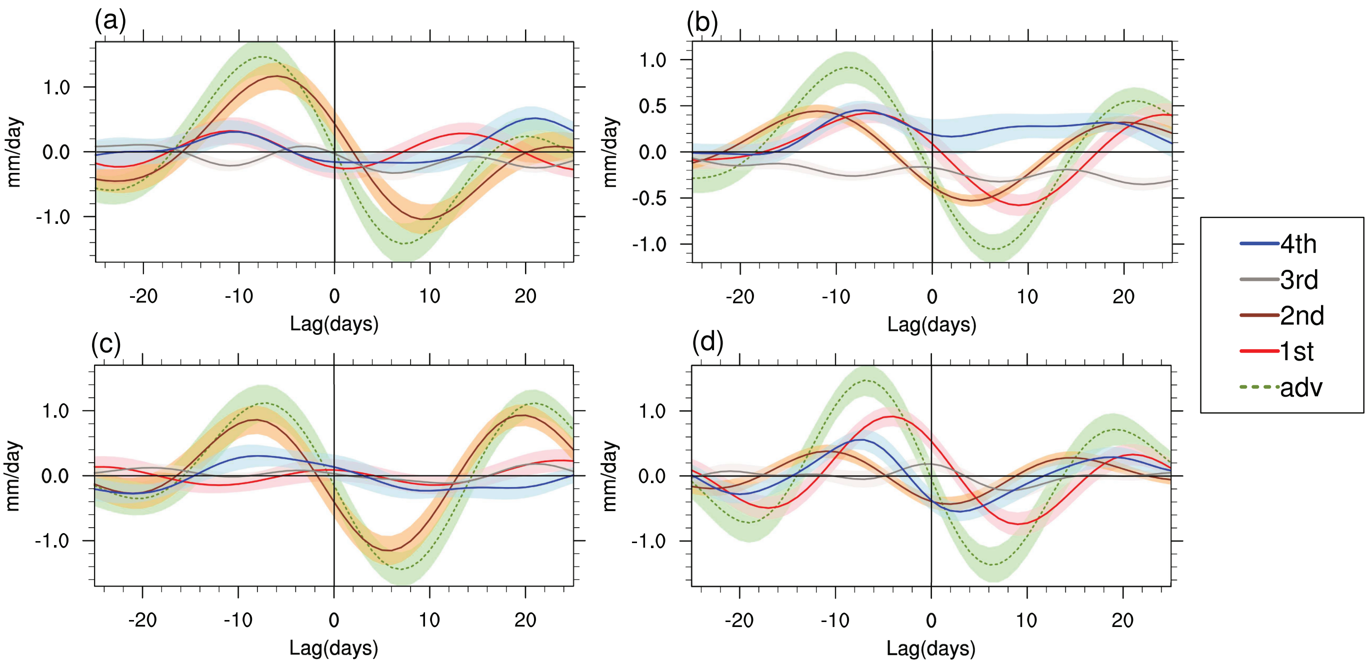

Figure 14. (a) Time series of different terms (ISO-filtered) of the advection equation (equation (7)) during the convective events over the AS from observations. Terms are calculated as described in the text. The dashed green line is advection as shown in Figure 9. (b) Same as (a) but for BoB. (c) Same as (a) but for model. (d) Same as (c) but for BoB. Units are given in mm/day. Shading along each line indicate the spread of the values normalized by the number of samples. First term $= \frac{1}{g}\int_{p_1}^{p_2}(-\mathbf{V}_h^c \cdot \nabla q')dp$, second term $= \frac{1}{g}\int_{p_1}^{p_2}(-\mathbf{V}_h' \cdot \nabla q^c)dp$, third term $= \frac{1}{g}\int_{p_1}^{p_2}(-\mathbf{V}_h' \cdot \nabla q')dp$, and fourth term = *residual*, as in the text.

($\frac{1}{g}\int_{p_1}^{p_2}(-\mathbf{V}_h' \cdot \nabla q^c)dp$) is advection due to anomalous wind associated with ISO acting on climatological moisture gradient. The third term ($\frac{1}{g}\int_{p_1}^{p_2}(-\mathbf{V}_h' \cdot \nabla q')dp$) represents advection due to ISO-filtered winds acting on ISO-filtered moisture gradient. The fourth term is residual, calculated by subtracting the first three terms in the right-hand side from the left-hand side. This term is not explained by the interaction between the ISO-filtered winds and moisture gradient or their interaction with climatological mean fields. Residual may arise primarily due to higher-frequency, transient variability.

The observations in Figure 14a show that the largest contribution of anomalous moisture advection over the AS region comes from the second term ($\frac{1}{g}\int_{p_1}^{p_2}(-\mathbf{V}_h' \cdot \nabla q^c)dp$) in equation (7). All the other terms show comparatively very less variability during the convective events over AS. In other words, advection due to anomalous winds associated with ISO acting on climatological moisture gradient works as a source of moisture over this region, which helps initiating instability in this region. Whereas along with the second term ($\frac{1}{g}\int_{p_1}^{p_2}(-\mathbf{V}_h' \cdot \nabla q^c)dp$), the first term ($\frac{1}{g}\int_{p_1}^{p_2}(-\mathbf{V}_h^c \cdot \nabla q')dp$) and the residual term also play a role in modulating the behavior of moisture advection over BoB (Figure 14b). The peak in $\frac{1}{g}\int_{p_1}^{p_2}(-\mathbf{V}_h' \cdot \nabla q^c)dp$ appears around 3–4 days before the peak in moisture advection over BoB. This is related with the establishment of low-level strong anomalous ISO-related easterlies over the BoB region approximately 15 days before the rainfall maxima (low-level wind structure is similar to the moisture transport vectors in Figure 11). Although the second term dominates the initial buildup of advection over the region, advection associated with the climatological horizontal wind acting on ISO-related anomalous moisture gradient and the residual term gradually dominates the behavior of advection in the later part before rainfall maxima over BoB. However, contribution from moisture advection toward the precipitation-evaporation (P-E) term is comparatively less over BoB compared to AS (Figures 9a and 9b).

The vertical profiles of moisture advection and the terms representing advection due to anomalous wind associated with ISO acting on climatological moisture gradient are shown for observations over AS and BoB in Figures 15a and 15b, respectively. Clearly, both moisture advection and $\frac{1}{g}\int_{p_1}^{p_2}(-\mathbf{V}_h' \cdot \nabla q^c)dp$ show maxima at nearly 875-hPa level over AS and BoB. However, the values over AS are relatively much higher (nearly four times at 850 hPa) than BoB. The peak in $\frac{1}{g}\int_{p_1}^{p_2}(-\mathbf{V}_h' \cdot \nabla q^c)dp$ is simultaneously located at a higher altitude (at 825 hPa) than advection over AS. However, two maxima in $\frac{1}{g}\int_{p_1}^{p_2}(-\mathbf{V}_h' \cdot \nabla q^c)dp$ over BoB are observed,

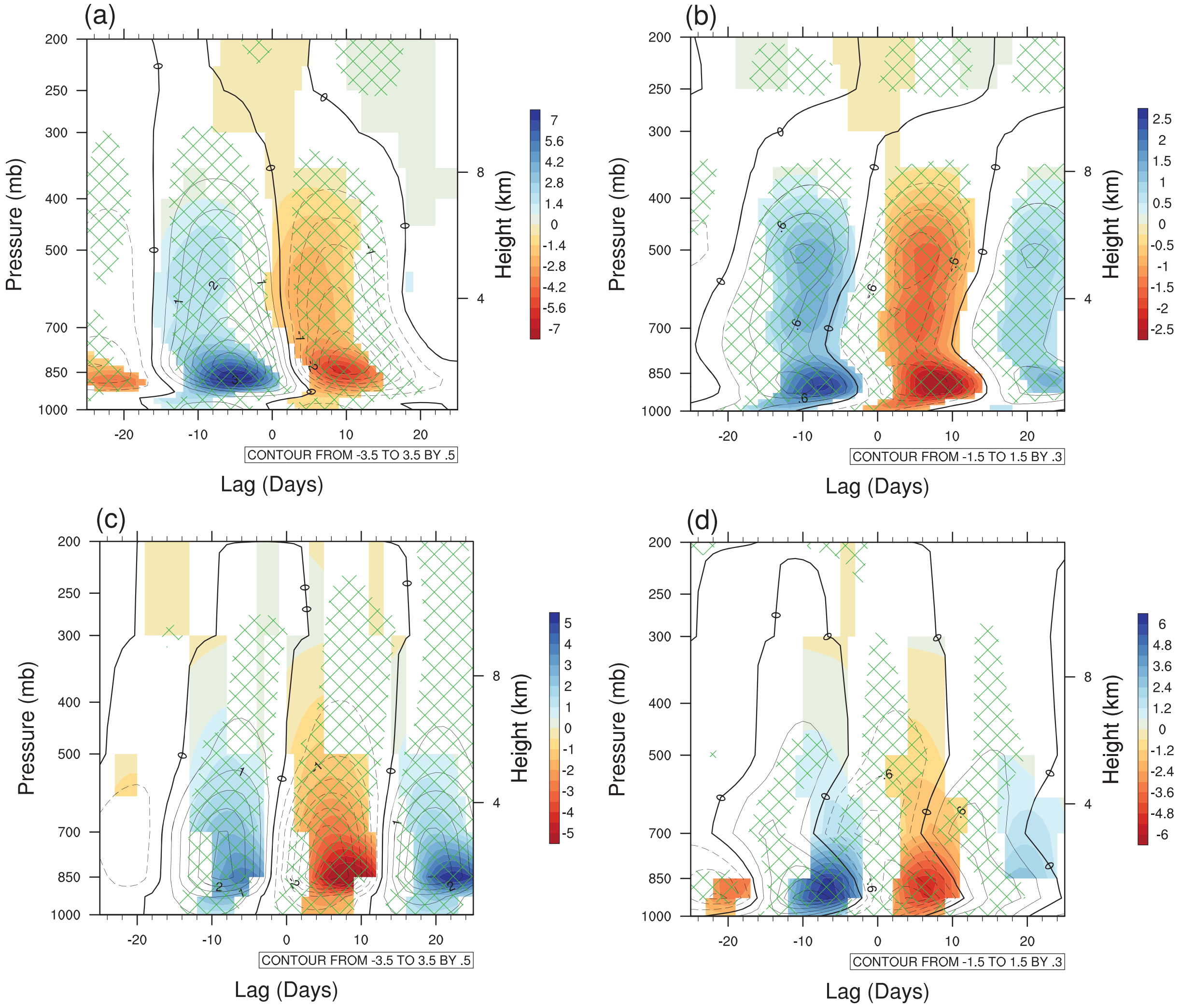

Figure 15. (a) Vertical profiles of ISO-filtered advection anomalies (color) and advection due to anomalous wind acting on climatological moisture gradient (second term in the advection equation; contours) during the convective events over the AS from observations. (b) Same as (a) but for BoB. (c) Same as (a) but for the model. (d) Same as (c) but for BoB. Units are given in $10^{-9} \times (\mathrm{kg/kg})\mathrm{s}^{-1}$. Advection anomalies significant at 5% level using a randomization test are shown in colors. Green hatched areas show where contour values are are significant at 5% level. Note the difference in color bars.

one at nearly 875 hPa and the other at 500 hPa. The lower maxima occurs nearly 4 days before the maxima in moisture advection. This is consistent with Figure 14b. The low-level maxima in advection over the AS is observed 5 days before the rainfall maxima, which comes after the advection maxima being observed over BoB (at Lag (−8)).

The RCM captures the largest contribution to anomalous advection from the advection due to anomalous wind associated with ISO acting on climatological moisture gradient over AS (Figure 14c). All other terms show relatively less variability. Similar to observations, the first term ($\frac{1}{g}\int_{p_1}^{p_2}(-\mathbf{V}_h^c \cdot \nabla q')dp$) and the residual term dominate the behavior of anomalous advection over BoB (Figure 14d). Although $\frac{1}{g}\int_{p_1}^{p_2}(-\mathbf{V}_h' \cdot \nabla q^c)dp$ shows the maxima earlier than the other terms over BoB, it appears to be of comparatively weaker magnitude. The vertical profiles of anomalous advection and $\frac{1}{g}\int_{p_1}^{p_2}(-\mathbf{V}_h' \cdot \nabla q^c)dp$ of equation (7) in the model show peaks in the lower troposphere at around 850-hPa level over AS (Figure 15c). These peaks are at a lower altitude (at nearly 900 hPa) over the BoB (Figure 15d), and also shows larger magnitude. This is consistent with Figures 14c and 14d, suggesting that anomalous advection over BoB shows comparatively higher variability over BoB than AS in the RCM. The vertical profile of advection over AS in the RCM is weaker than in observations possibly because of the representation of climatological moisture gradient in the model.

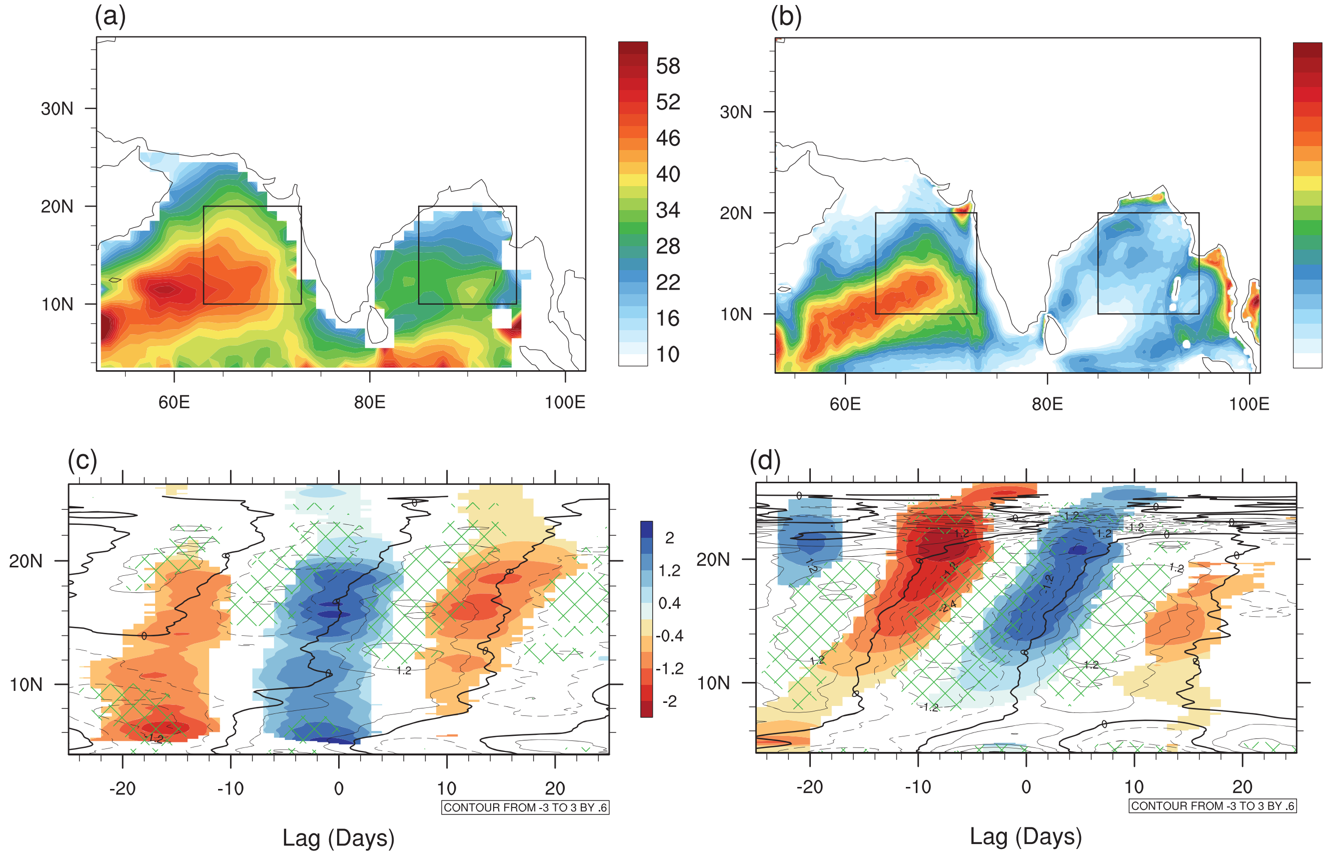

Figure 16. (a) May–October mean mixed layer depth (MLD) from mixed layer climatology and database. (b) Same as (a) but for the model. Boxes indicate the AS and BoB boxes used in this study. (c) Lag-latitude diagrams of ISO in rainfall (in colors) and ISO-filtered MLD from model (in contours; negative values in dashed contours) averaged over AS longitudes during the convective events. (d) Same as (c) but for BoB longitudes. Rainfall anomalies significant at 5% level using a randomization test are shown in colors. Green hatched areas show where MLDs are significant at 5% level.

3.7. MLD in the Model

One of the reasons for validating the model thus far is not only to display the model fidelity in terms of its ISO simulation but also to assess the role of the MLD in the differential propagation of the ISO in AS and BoB. The model provides a high temporal and spatial resolution data on the upper ocean that is consistent with the coupled evolution of the ISM unmatched by any observations.

The above analysis in the previous subsections clearly suggests that the northward propagation of convection slows down over BoB, whereas it propagates at a faster rate over the AS. This is possibly associated with a strong coupling between ocean and atmosphere occurring over BoB; a shallow MLD could be favorable for increased ocean-atmosphere interaction. Intraseasonal variability in subsurface variables like MLD is observed over the Indian Ocean (D. E. Waliser et al., 2004; Y. Li et al., 2016), and the model performs reasonably well in simulating subsurface intraseasonal variability (Misra et al., 2018). In Figures 16a and 16b, we show May–October climatological mean MLD for observations (Holte et al., 2017) and model, respectively. The model captures the distribution of MLD over the domain but shows relatively less amplitude. It is quite evident from both model and observation that MLD over BoB is much shallower than in AS. Especially, freshwater influx from several rivers make the MLD even shallower over the northern BoB. Generally, intraseasonal variability in SST is reported to be larger over the regions with shallower MLD (Duvel & Vialard, 2007). In other words, shallower MLD favors an increase in surface temperature for a similar amount of radiation flux. This, in turn, could enhance surface latent heat flux and evaporation making the lower atmosphere unstable. Thus, a stronger ISO signal over BoB might be associated with a shallower MLD. However, in Figures 3a and 3b, we found that the magnitude of SST in the intraseasonal timescale during the convective events is higher over the AS as compared to BoB. Changes in surface temperature is related not only to the heat flux forcing but also to the effect of interior ocean and zonal and meridional advections of the mixed layer currents (Duvel et al., 2004; Duvel & Vialard, 2007). It is extremely difficult to assess the role of the different processes in the variability of SST in ISO timescale without the precise measurements on the variability of the mixed layer structure. Thus, it is quite revealing at this point that although the MLD is deeper over AS, the magnitude of SST variability in ISO timescale is relatively higher over this region during strong convective events (Figures 3a and 3b).

In Figures 16c and 16d, we show lag-latitude diagrams for ISO-filtered rainfall and MLD in the RCM over AS and BoB, respectively. MLD in both the ocean basins shows northward propagation, with stronger variability over BoB. Negative anomalies in MLD leads positive rainfall anomalies by around a week over BoB, suggesting a development of a shallower MLD before convection initiates. MLD and rainfall both show nearly similar speed over the BoB, but the speed of propagation is different over AS. MLD leads rainfall by nearly 16 days at 6° N, but the lead time reduces to 5 days at 20° N. Soon after rainfall begins, MLD anomalies change sign and become positive. The propagation speed of MLD in the RCM is consistent with the corresponding propagation characteristics observed in SST (Figure 3). This analysis suggest that the speed of the propagation of rainfall anomalies over the northern AS is not strongly associated with the subsurface ocean conditions. Therefore, this regional coupled simulation suggests that the northwest-southeast tilt of ISO is a phenomenon forced by the atmospheric processes of moisture advection with the upper ocean playing a passive role.

4. Conclusions and Discussions

In this study, we provide an insight on how propagation of ISO rainfall during boreal summer differs over the oceanic basins adjacent to India: AS and BoB. Although the amount of seasonal mean rainfall over the AS is lower than over BoB, rainfall, SST, and other fields show significant amount of variability over the AS region. Northward propagation of rainfall in intraseasonal timescale is often seen as ITCZ moving northward from the equatorial region every 2–6 weeks (Gadgil, 2003). How this east-west oriented structure of convection propagates northward and what causes this convective band tilted in a northwest-southeast direction when it moves to the central Indian latitudes remain elusive. Many theories have been put forward to understand the mechanism of this northward propagation using both observational analysis and numerical modeling studies (brief discussion on many of these theories can be found in Webster et al., 1998, B. N. Goswami, 2005 and R S. Nanjundiah and Krishnamurti, 2007). However, there are very limited investigations on understanding the differences in the nature of ISO over the two ocean basins and whether this difference put forth the tilted band of convection over the Indian region.

We used satellite-derived rainfall products, and other observational products including ERA-Interim reanalysis data during 1998–2014 in this study, and tested the results with a high-resolution RCM simulation of 10 years. A data-adaptive technique, MSSA is used to extract ISO from the data. We identified strong convective events over the AS (39 events in observation) and BoB (63 events in observation) and then compared the composite structures of ISO propagation during these convective events over these two ocean basins. We found that ISO in rainfall propagates at a much faster rate once it reaches the central AS than over BoB. ISO in rainfall propagates at a speed of nearly 1.25°/day over AS, but the speed is 0.74°/day over BoB. This faster propagation rate could be responsible in determining the tilted structure of convective band in the northward propagating ITCZ. It is found that SST and subsurface variables like MLD show nearly similar speed in both the ocean basins, suggesting that atmospheric processes could play a major role in rainfall over the AS. Theories suggest that in the presence of strong easterly vertical shear, barotropic vorticity to the north of an existing convection is essential for moisture convergence, which helps move existing convection northward. However, both barotropic vorticity and low-level convergence show a slower speed than ISO rainfall over AS. Therefore, the rainfall over the AS could be dictated by thermodynamics and the moisture in the atmospheric column. We found that faster propagation in rainfall could be explained by horizontal MFC, which is a very useful parameter to determine convective instability and can be determined using the moisture budget equation. MFC can be partitioned into two terms, moisture advection and moisture convergence, and largely, the balance of these two terms determine the precipitation minus evaporation quantity. Vertically integrated intraseasonal moisture convergence shows variations along with rainfall and shows nearly similar values over AS and BoB. However, moisture advection shows a peak nearly a week before the rainfall maxima and is significantly high over AS than BoB. Upon further investigation, it is found that advection due to anomalous wind associated with ISO acting on climatological moisture gradient plays a crucial role in transporting moisture to AS, a week before the rainfall peaks. Typically, break-like conditions persist over central India a week before this rainfall maxima, and low-level winds are easterly over the southern peninsular India. Vertical and spatial maps of moisture transport show anomalous moisture being advected from South China Sea and BoB over this region, especially in the lower troposphere (875 hPa). This positive moisture anomaly acts to increase the low-level moist static energy and destabilize the atmosphere (less vertical moist stability), which, in turn, generates convection. Over BoB, rainfall is strongly coupled with the oceanic processes, and the MLD over this region is relatively shallow. Atmospheric instability over BoB starts to develop soon after a maxima in downward shortwave radiation flux anomaly. Vertical moist stability in the atmosphere shows a minima nearly 2 weeks before rainfall maxima. Moisture advection in intraseasonal timescale plays a relatively smaller role in determining the variability in rainfall over BoB. Convection over the BoB is largely driven by the changes in surface heat fluxes.

We tested these results using a RCM forced with boundary conditions from reanalysis data sets. The RCM captures the seasonal mean patterns of rainfall reasonably well. Intraseasonal northward propagation of rainfall is also captured, especially over BoB, albeit with a faster speed and lesser amplitude. In the composite analysis done with the model rainfall data, it shows distinct ISO propagation speed over AS (∼2°/day) and BoB (∼1°/day), with ISO-filtered SST propagating nearly at the same speed over the two oceanic regions (∼1°/day). MFC in the model also shows a very good agreement with the propagation of rainfall. The horizontal moisture advection in the RCM shows increased values over both AS and BoB, nearly a week before rainfall maxima. However, contrary to observations the amount of moisture advection at intraseasonal timescales is nearly similar over both the ocean basins. Also, local rate of change in moisture over both AS and BoB is not negligible in the RCM, as it was in the observations. However, the contribution from advection due to anomalous wind associated with ISO acting on climatological moisture gradient term to the total anomalous advection over AS is well captured in the model. By and large, the RCM has simulated many of the important intraseasonal characteristics responsible for faster propagation of ISO-filtered rainfall over the AS.

The fidelity of the model in simulating ISO is presented largely to investigate model subsurface conditions in the context of differential ISO rainfall speed over AS and BoB. The RCM provides high-resolution MLD data, unmatched by any observations, to examine the daily evolution of subsurface conditions over the ocean basins. It is found that similar to SST, the speed of ISO-filtered MLD over AS is slower than ISO-filtered rainfall, suggesting the northward propagation of rainfall largely depends upon atmospheric processes, especially anomalous moisture advection from the eastern side of the domain. Seasonal mean MLD over the AS is higher than in BoB.

This study highlights the importance of atmospheric moisture advection in modulating the nature of active-break spells over the Indian region. Prasanna and Annamalai (2012) suggested that dry advection 15 days before negative rainfall anomalies develop plays the principal role in initiating extended break phase over India. Regional anticyclonic circulation anomalies and rainfall anomalies work together to advect air with low moist static energy content from the north to central India. They also showed the dominance of anomalous wind acting on climatological moisture gradient term in the advection equation. In our study, it is confirmed that the rainfall amount over both the ocean basins are preceded by increased moisture advection. However, over the northern AS, it is an important factor that brings anomalously large quantity of moisture, which destabilizes the atmosphere. Convection over AS is largely modulated by the arrival of this anomalous moisture advection. Our results imply that better understanding of atmospheric moisture distribution over the Indian region is necessary to unravel exact nature of the tilted structure in ISO propagation. Our model simulation results show that the upper ocean of either AS or BoB does not contribute to this observed tilt of the ISO.

Appendix A: Calculating phase speed of ISO

Calculation of the speed of the northward propagation is done by choosing maxima that occurs within 25 days of the reference time (Lag 0 as defined earlier). The speeds are calculated for each time-latitude section over the AS (63° E to 73° E) or BoB (85° E to 95° E) longitudes by averaging the ISO-filtered anomaly fields across the latitude intervals from 5° N to 10° N, 10° N to 15° N, 15° N to 20° N, 20° N to 25° N, and 25° N to 30° N. For each field, the time when a maxima occurs within each latitude band is calculated. The speed of the northward propagation of any field is determined by linear least squares fit on the time in which a maxima occurs within each latitude band. Northward propagation can be difficult to capture at times, especially for "noisy" variables like rainfall. Therefore, to calculate the speed of the northward propagation, we consider only northward moving signals and do not consider cases when we find few instances of southward or no movement. The results presented here qualitatively agree if we slightly increase (6° and 7°) or decrease (3° and 4°) the latitudinal extent of the sizes of the boxes taken in this analysis.

Appendix B: Conversion of energy flux to water flux

Conversion of surface energy flux (H_f) to water flux (W_f) can be done using the following formula:

$$H_f = \rho \times L_v \times W_f, \tag{B1}$$

where ρ is the density of water and L_v is the latent heat of vaporization. Over the Indian region, where surface temperature is nearly 30 ° C, the values of ρ and L_v can be considered as 995.7 kg/m^3 and 2,429,900 J/kg. Thus, for every 1 mm/day of water flux, the equivalent radiation flux can be computed as

$$W/m^2 = 995.7\ \mathrm{kg/m^3} \times 2429900\ \mathrm{J/kg} \times 1\ \mathrm{mm/day} \times (1/86400)\ \mathrm{day/s} \times (1/1000)\ \mathrm{mm/m} \tag{B2}$$

or

$$28.00\ \mathrm{W/m^2} = 1\ \mathrm{mm/day}. \tag{B3}$$

Following this and given the fact that all the analyses are done using daily data, vertically integrated moist static energy or vertical moist stability of the atmosphere measured in units J/m^2 can be converted to mm/day as 1 mm/day = 86,400 × 28.00 J/m^2.

Acknowledgments
The authors acknowledge NASA for making TRMM rainfall data available (https://pmm.nasa.gov/TRMM), ECMWF for the ERA-Interim data set (https://apps.ecmwf.int/datasets/), and NOAA ESRL PSD for OISST data set (https://www.esrl.noaa.gov/psd/data/). Mixed layer climatology is obtained online (from http://mixedlayer.ucsd.edu/). Model simulation data sets used in this study can be downloaded from the OSF website (https://osf.io/qyvsw/). This work is funded by NASA Grants NNX17AG72G and NNX16AD83G, NSF Award 1606296, and the Earth System Science Organization, Ministry of Earth Sciences, Government of India (MM/SERP/FSU/2014/SSC-02/002).

References

Achuthavarier, D., & Krishnamurthy, V. (2011). Role of Indian and Pacific SST in Indian summer monsoon intraseasonal variability. *Journal of Climate*, *24*(12), 2915–2930.

Ajaya Mohan, R., & Goswami, B. N. (2003). Potential predictability of the Asian summer monsoon on monthly and seasonal time scales. *Meteorology and Atmospheric Physics*, *84*(1-2), 83–100. https://doi.org/10.1007/s00703-002-0576-4

Allen, M., & Robertson, A. (1996). Distinguishing modulated oscillations from coloured noise in multivariate datasets. *Climate Dynamics*, *12*(11), 775–784. https://doi.org/10.1007/s003820050142

Alpert, J. C., Kanamitsu, M., Caplan, P. M., Sela, J. G., White, G., & Kalnay, E. (1988). Mountain induced gravity wave drag parameterization in the NMC medium-range forecast model. In *Proc. 8th conf. on numerical weather predic- tion* (pp. 726–733). Baltimore, MD: Amer. Meteor. Soc.

Annamalai, H. (2010). Moist dynamical linkage between the equatorial Indian Ocean and the South Asian monsoon trough. *Journal of the Atmospheric Sciences*, *67*(3), 589–610.

Annamalai, H., & Slingo, J. M. (2001). Active/break cycles: diagnosis of the in- traseasonal variability of the Asian summer monsoon. *Climate Dynamics*, *18*(1-2), 85–102. https://doi.org/10.1007/s003820100161

Banacos, P. C., & Schultz, D. M. (2005). The use of moisture flux convergence in forecasting convective initiation: Historical and operational perspectives. *Weather and Forecasting*, *20*(3), 351–366.

Boyer Montegut, C., Madec, G., Fischer, A. S., Lazar, A., & Iudicone, D. (2004). Mixed layer depth over the global ocean: An examination of profile data and a profile-based climatology. *Journal of Geophysical Research, Oceans*, *109*(C12).

Carton, J. A., & Giese, B. S. (2008). A Reanalysis of Ocean Climate Using Simple Ocean Data Assimilation (SODA). *Monthly Weather Review*, *136*(8), 2999–3017. https://doi.org/10.1175/2007MWR1978.1

Chou, M.-D., Lee, K.-T., Tsay, S.-C., & Fu, Q. (1999). Parameterization for cloud longwave scattering for use in atmospheric models. *Journal of Climate*, *12*(1), 159–169. https://doi.org/10.1175/1520-0442(1999)012(0159:PFCLSF)2.0.CO;2

Chou, M. D., & Suarez, M. J. (1994, 03). *An efficient thermal infrared radiation pa- rameterization for use in general circulation models* (Tech. Rep.). NASA Tech. Memo. NASA-TM-104606.

Dash, S., Shekhar, M., & Singh, G. (2006). Simulation of Indian summer monsoon circulation and rainfall using RegCM3. *Theoretical and Applied Climatology*, *86*(1-4), 161–172.

Dee, D., Uppala, S., Simmons, A., Berrisford, P., Poli, P., Kobayashi, S., et al. (2011). The ERA-Interim reanalysis: Configuration and performance of the data assimilation system. *Quarterly Journal of the Royal Meteorological Society*, *137*(656), 553–597. https://doi.org/10.1002/qj.828

DeMott, C. A., Stan, C., & Randall, D. A. (2013). Northward propagation mecha- nisms of the boreal summer intraseasonal oscillation in the ERA-Interim and SP-CCSM. *Journal of Climate*, *26*(6), 1973–1992.

Duvel, J. P., Roca, R., & Vialard, J. (2004). Ocean mixed layer temperature varia- tions induced by intraseasonal convective perturbations over the indian ocean. *Journal of the Atmospheric Sciences*, *61*(9), 1004–1023.

Duvel, J. P., & Vialard, J. (2007). Indo-pacific sea surface temperature perturba- tions associated with intraseasonal oscillations of tropical convection. *Journal of Climate*, *20*(13), 3056–3082.

Ek, M., Mitchell, K., Lin, Y., Rogers, E., Grunmann, P., Koren, V., et al. (2003). Implementation of Noah land surface model advances in the National Centers for Environmental Prediction operational mesoscale Eta model. *Journal of Geophysical Research*, *108*(D22), 8851. https://doi.org/10.1029/2002JD003296

Fu, X., & Wang, B. (2004). The boreal-summer intraseasonal oscillations simulated in a hybrid coupled atmosphere-ocean model. *Monthly Weather Review*, *132*(11), 2628–2649.

Gadgil, S. (2003). The Indian monsoon and its variability. *Annual Review of Earth and Planetary Sciences*, *31*(1), 429–467. https://doi.org/10.1146/annurev.earth.31.100901.141251

Gao, Y., Klingaman, N. P., DeMott, C. A., & Hsu, P.-C. (2019). Diagnosing ocean feedbacks to the bsiso: Sst-modulated surface fluxes and the moist static energy budget. *Journal of Geophysical Research: Atmospheres*, *124*, 146–170. https://doi.org/10.1029/2018JD029303

Ghil, M., Allen, M., Dettinger, M., Ide, K., Kondrashov, D., Mann, M., et al. (2002). Advanced spectral methods for climatic time series. *Reviews of Geophysics*, *40*(1), 1003. https://doi.org/10.1029/2000RG000092

Glazer, R. H., & Misra, V. (2018). Ice versus liquid water saturation in simulations of the Indian summer monsoon. *Climate Dynamics*, *51*(9-10), 3847–3863.

Goswami, B., & Shukla, J. (1984). Quasi-periodic oscillations in a symmetric general circulation model. *Journal of the Atmospheric Sciences*, *41*(1), 20–37.

Goswami, B. N. (2005). South asian monsoon. In K. M. Lau, & D. E. Waliser (Eds.), *Intraseasonal variability in the atmosphere-ocean climate system* (pp. 19–61). Praxis: Springer.

Holte, J., Talley, L. D., Gilson, J., & Roemmich, D. (2017). An Argo mixed layer cli- matology and database. *Geophysical Research Letters*, *44*(11), 5618–5626.

Hong, S.-Y., & Pan, H.-L. (1996). Nonlocal boundary layer vertical diffusion in a medium-range forecast model. *Monthly Weather Review*, *124*(10), 2322–2339. https://doi.org/10.1175/1520-0493(1996)124(2322:NBLVDI)2.0.CO;2

Huffman, G. J., Bolvin, D. T., Nelkin, E. J., Wolff, D. B., Adler, R. F., Gu, G., et al. (2007). The TRMM multisatellite precipitation analysis (TMPA): Quasi-global, multiyear, combined-sensor precipitation estimates at fine scales. *Journal of Hydrometeorology*, *8*(1), 38–55. https://doi.org/10.1175/JHM560.1

Jiang, X., Li, T., & Wang, B. (2004). Structures and mechanisms of the north- ward propagating boreal summer intraseasonal oscillation. *Journal of Climate*, *17*(5), 1022–1039. https://doi.org/10.1175/1520-0442(2004)017(1022:SAMOTN)2.0.CO;2

Juang, H.-M. H., & Kanamitsu, M. (1994). The nmc nested regional spectral model. *Monthly Weather Review*, *122*(1), 3–26.

Kanamitsu, M., Ebisuzaki, W., Woollen, J., Yang, S.-K., Hnilo, J., Fiorino, M., & Potter, G. (2002). NCEPDOE AMIP-II Reanalysis (R-2). *Bulletin of the American Meteorological Society*, *83*(11), 1631–1644. https://doi.org/10.1175/BAMS-83-11-1631

Kanamitsu, M., Yoshimura, K., Yhang, Y.-B., & Hong, S.-Y. (2010). Errors of in- terannual variability and trend in dynamical downscaling of reanalysis. *Journal of Geophysical Research: Atmospheres*, *115*, D17115. https://doi.org/10.1029/2009JD013511

Karmakar, N., Chakraborty, A., & Nanjundiah, R. S. (2017). Space-Time Evolution of the Low- and High-Frequency Intraseasonal Modes of the Indian Summer Monsoon. *Monthly Weather Review*, *145*(2), 413–435. https://doi.org/10.1175/MWR-D-16-0075.1

Karmakar, N., & Krishnamurti, T. N. (2019). Characteristics of north- ward propagating intraseasonal oscillation in the indian summer monsoon. *Climate Dynamics*, *52*(3), 1903–1916. Retrieved from. https://doi.org/10.1007/s00382-018-4268-2

Kemball-Cook, S., & Wang, B. (2001). Equatorial waves and air-sea interaction in the boreal summer intraseasonal oscillation. *Journal of Climate*, *14*(13), 2923–2942. https://doi.org/10.1175/1520-0442(2001)014

Klingaman, N. P., Inness, P. M., Weller, H., & Slingo, J. M. (2008). The impor- tance of high-frequency sea surface temperature variability to the intraseasonal oscillation of Indian monsoon rainfall. *Journal of Climate*, *21*(23), 6119–6140.

Klingaman, N. P., Weller, H., Slingo, J. M., & Inness, P. M. (2008). The intrasea- sonal variability of the Indian summer monsoon using TMI sea surface temper- atures and ECMWF reanalysis. *Journal of Climate*, *21*(11), 2519–2539.

Klingaman, N. P., Woolnough, S. J., Weller, H., & Slingo, J. M. (2011). The im- pact of finer-resolution air–sea coupling on the intraseasonal oscillation of the Indian monsoon. *Journal of Climate*, *24*(10), 2451–2468.

Krishnamurthy, V., & Kirtman, B. P. (2009). Relation between Indian monsoon variability and SST. *Journal of Climate*, *22*(17), 4437–4458.

Krishnamurthy, V., & Shukla, J. (2007). Intraseasonal and seasonally persisting pat- terns of Indian monsoon rainfall. *Journal of Climate*, *20*(1), 3–20. https://doi.org/10.1175/JCLI3981.1

Large, W. G., McWilliams, J. C., & Doney, S. C. (1994). Oceanic vertical mixing: A review and a model with a nonlocal boundary layer parameterization. *Reviews of Geophysics*, *32*(4), 363–403.

Lee, J.-Y., Wang, B., Wheeler, M. C., Fu, X., Waliser, D. E., & Kang, I.-S. (2013). Real-time multivariate indices for the boreal summer intraseasonal oscillation over the Asian summer monsoon region. *Climate Dynamics*, *40*(1-2), 493–509.

Li, H., & Misra, V. (2014, Nov 01). Thirty-two-year ocean–atmosphere coupled downscaling of global reanalysis over the intra-american seas. *Climate Dynamics*, *43*(9), 2471–2489. https://doi.org/10.1007/s00382-014-2069-9

Li, Y., Han, W., Wang, W., & Ravichandran, M. (2016). Intraseasonal variability of SST and precipitation in the Arabian Sea during the Indian summer monsoon: Impact of ocean mixed layer depth. *Journal of Climate*, *29*(21), 7889–7910.

Mellor, G. L., & Yamada, T. (1982). Development of a turbulence closure model for geophysical fluid problems. *Reviews of Geophysics*, *20*(4), 851–875.

Misra, V., Mishra, A., & Bhardwaj, A. (2017). High-resolution regional-coupled ocean–atmosphere simulation of the indian summer monsoon. *International Journal of Climatology*, *37*(S1), 717–740.

Misra, V., Mishra, A., & Bhardwaj, A. (2018). Simulation of the intraseasonal vari- ations of the indian summer monsoon in a regional coupled oceanatmosphere model. *Journal of Climate*, *31*(8), 3167–3185. https://doi.org/10.1175/JCLI-D-17-0434.1

Moorthi, S., & Suarez, M. J. (1992). Relaxed arakawa-schubert. a parameterization of moist convection for general circulation models. *Monthly Weather Review*, *120*(6), 978–1002. https://doi.org/10.1175/1520-0493(1992)120(0978:RASAPO)2.0.CO;2

Moron, V., Robertson, A., & Ghil, M. (2012). Impact of the modulated an- nual cycle and intraseasonal oscillation on daily-to-interannual rainfall vari- ability across monsoonal India. *Climate Dynamics*, *38* (11-12), 2409-2435. Re- trieved from https://doi.org/10.1007/s00382-011-1253-4.

Moron, V., Vautard, R., & Ghil, M. (1998). Trends, interdecadal and interannual oscillations in global sea-surface temperatures. *Climate Dynamics*, *14*(7-8), 545–569. https://doi.org/10.1007/s003820050241

Nanjundiah, R., Srinivasan, J., & Gadgil, S. (1992). Intraseasonal variation of the Indian summer monsoon. II. Theoretical aspects. *Journal of the Meteorological Society of Japan*, *70*, 529–550.

Nanjundiah, R. S., & Krishnamurti, T. (2007). Intraseasonal oscillation of tropical convergence zones: Theory and prediction. *Current Science*, 173–181.

Neelin, J. D., & Held, I. M. (1987). Modeling tropical convergence based on the moist static energy budget. *Monthly Weather Review*, *115*(1), 3–12.

Pillai, P. A., & Sahai, A. (2014). Moist dynamics of active/break cycle of Indian summer monsoon rainfall from NCEPR2 and MERRA reanalysis. *International Journal of Climatology*, *34*(5), 1429–1444.

Pillai, P. A., & Sahai, A. K. (2016). Moisture dynamics of the northward and eastward propagating boreal summer intraseasonal oscillations: possible role of tropical Indo-west Pacific SST and circulation. *Climate Dynamics*, *47*(3-4), 1335–1350.

Plaut, G., & Vautard, R. (1994). Spells of low-frequency oscillations and weather regimes in the Northern Hemisphere. *Journal of the Atmospheric Sciences*, *51*(2), 210–236. https://doi.org/10.1175/1520-0469(1994)051

Prasanna, V., & Annamalai, H. (2012). Moist dynamics of extended monsoon breaks over South Asia. *Journal of Climate*, *25*(11), 3810–3831.

Raj Parampil, S., Bharathraj, G., Harrison, M., & Sengupta, D. (2016). Observed subseasonal variability of heat flux and the sst response of the tropical indian ocean. *Journal of Geophysical Research: Oceans*, *121*, 7290–7307. https://doi.org/10.1002/2016JC011948

Rajeevan, M. (2001). Prediction of Indian summer monsoon: Status, problems and prospects. *Current Science*, *81*(11), 1451–1458.

Rajeevan, M., Gadgil, S., & Bhate, J. (2010). Active and break spells of the Indian summer monsoon. *Journal of Earth System Science*, *119*(3), 229–247. https://doi.org/10.1007/s12040-010-0019-4

Rajendran, K., Gadgil, S., & Surendran, S. (2018). Monsoon season local control on precipitation over warm tropical oceans. *Meteorology and Atmospheric Physics*, 1–15.

Rajendran, K., & Kitoh, A. (2006). Modulation of tropical intraseasonal oscillations by ocean–atmosphere coupling. *Journal of Climate*, *19*(3), 366–391.

Raju, A., Parekh, A., Chowdary, J., & Gnanaseelan, C. (2015). Assessment of the Indian summer monsoon in the WRF regional climate model. *Climate Dynamics*, *44*(11-12), 3077–3100.

Reynolds, R. W., Smith, T. M., Liu, C., Chelton, D. B., Casey, K. S., & Schlax, M. G. (2007). Daily high-resolution-blended analyses for sea surface tempera- ture. *Journal of Climate*, *20*(22), 5473–5496. https://doi.org/10.1175/2007JCLI1824.1

Roxy, M., Tanimoto, Y., Preethi, B., Terray, P., & Krishnan, R. (2013). Intrasea- sonal SST-precipitation relationship and its spatial variability over the tropical summer monsoon region. *Climate Dynamics*, *41*(1), 45–61.

Sabeerali, C., Ramu Dandi, A., Dhakate, A., Salunke, K., Mahapatra, S., & Rao, S. A. (2013). Simulation of boreal summer intraseasonal oscillations in the latest CMIP5 coupled GCMs. *Journal of Geophysical Research: Atmospheres*, *118*, 4401–4420. https://doi.org/10.1002/jgrd.50403

Sharmila, S., Pillai, P., Joseph, S., Roxy, M., Krishna, R., Chattopadhyay, R., et al. (2013). Role of ocean–atmosphere interaction on northward prop- agation of Indian summer monsoon intra-seasonal oscillations (MISO). *Climate Dynamics*, *41*(5-6), 1651–1669. https://doi.org/10.1007/s00382-013-1854-1

Shchepetkin, A. F., & McWilliams, J. C. (2005). The regional oceanic modeling system (ROMS): a split-explicit, free-surface, topography-following-coordinate oceanic model. *Ocean Modelling*, *9*(4), 347–404.

Shige, S., Nakano, Y., & Yamamoto, M. K. (2017). Role of orography, diurnal cycle, and intraseasonal oscillation in summer monsoon rainfall over the Western Ghats and Myanmar Coast. *Journal of Climate*, *30*(23), 9365–9381.

Sikka, D., & Gadgil, S. (1980). On the maximum cloud zone and the ITCZ over Indian, longitudes during the southwest monsoon. *Monthly Weather Review*, *108*(11), 1840–1853. https://doi.org/10.1175/1520-0493(1980)108(1840:OTMCZA)2.0.CO;2

Sperber, K. R., Annamalai, H., Kang, I.-S., Kitoh, A., Moise, A., Turner, A., et al. (2013). The Asian summer monsoon: an intercomparison of CMIP5 vs. CMIP3 simulations of the late 20th century. *Climate Dynamics*, *41*(9-10), 2711–2744. https://doi.org/10.1007/s00382-012-1607-6

Sperber, K. R., Brankovic, C., Deque, M., Frederiksen, C., Graham, R., Kitoh, A., et al. (2001). Dynamical seasonal predictability of the Asian summer monsoon. *Monthly Weather Review*, *129*(9), 2226–2248. https://doi.org/10.1175/1520-0493(2001)129(2226:DSPOTA)2.0.CO;2

Srinivasan, J., Gadgil, S., & Webster, P. (1993). Meridional propagation of large- scale monsoon convective zones. *Meteorology and Atmospheric Physics*, *52*(1-2), 15–35.

Srinivasan, J., & Smith, G. (1996). The role of heat fluxes and moist static energy in tropical convergence zones. *Monthly Weather Review*, *124*(10), 2089–2099.

Tiedtke, M. (1983). The sensitivity of the time-mean large-scale flow to cumulus convection in the ECMWF model. In *Workshop on convection in large-scale numerical models, 28 november to 1 december 1983* (pp. 297–316). Shinfield Park, Reading: ECMWF.

Umakanth, U., Kesarkar, A. P., Raju, A., & Rao, S. V. B. (2016). Representation of monsoon intraseasonal oscillations in regional climate model: sensitivity to convective physics. *Climate Dynamics*, *47*(3-4), 895–917.

Umlauf, L., & Burchard, H. (2003). A generic length-scale equation for geophysical turbulence models. *Journal of Marine Research*, *61*(2), 235–265.

Waliser, D., Jin, K., Kang, I.-S., Stern, W., Schubert, S., Wu, M., et al. (2003). AGCM simulations of intraseasonal variability associated with the Asian sum-mer monsoon. *Climate Dynamics*, *21*(5-6), 423–446. https://doi.org/10.1007/s00382-003-0337-1

Waliser, D. E., Murtugudde, R., & Lucas, L. E. (2004). Indo-Pacific Ocean response to atmospheric intraseasonal variability: 2. Boreal summer and the Intrasea- sonal Oscillation. *Journal of Geophysical Research*, *109*, C03030. https://doi.org/10.1029/2003JC002002

Wang, B., & Xie, X. (1997). A model for the boreal summer intraseasonal oscilla- tion. *Journal of the Atmospheric Sciences*, *54*(1), 72–86.

Webster, P. J. (1983). Mechanisms of monsoon low-frequency variability: Surface hydrological effects. *Journal of the Atmospheric Sciences*, *40*(9), 2110–2124.

Webster, P. J., Magana, V. O., Palmer, T. N., Shukla, J., Tomas, R. A., Yanai, M., & Yasunari, T. (1998). Monsoons: Processes, predictability, and the prospects for prediction. *Journal of Geophysical Research*, *103*(C7), 14,451–145,10. https://doi.org/10.1029/97JC02719

Yasunari, T. (1979). Cloudiness fluctuations associated with the Northern Hemi- sphere summer monsoon. *Journal of the Meteorological Society of Japan*, *57*(3), 227–242.

Zhao, Q., & Carr, F. H. (1997). A prognostic cloud scheme for operational nwp models. *Monthly Weather Review*, *125*(8), 1931–1953. https://doi.org/10.1175/1520-0493(1997)125(1931:APCSFO)2.0.CO;2